Multi-mode interactions in vortex-induced vibrations of flexible curved/straight structures with geometric nonlinearities

Narakorn Srinil*

Department of Naval Architecture and Marine Engineering, University of Strathclyde, Henry Dyer Building, Glasgow G4 0LZ, Scotland, UK

Abstract

A general low-order fluid–structure interaction model capable of evaluating the multi-mode interactions in vortex-induced vibrations of flexible curved/straight structures is presented. Cross-flow motions due to unsteady lift forces of inclined sagged cables and tensioned beams in uniform currents are investigated. In contrast to a linear equation governing the transverse motion of straight beams or cables typically considered in the literature, coupled horizontal/vertical (axial/transverse) displacements and geometric nonlinearities of curved cable (straight beam) are accounted for. A distributed nonlinear wake oscillator is considered in the approximation of space–time varying hydrodynamics. This semi-empirical fluid force model in general depends on the mass-damping parameter and has further been modified to capture both the effects of varying initial curvatures of the inclined cylinder and the Reynolds number. Numerical simulations are performed in the case of varying flow velocities and parametric results highlight several meaningful aspects of vortex-induced vibrations of long flexible cylinders. These comprise multi-mode lock-in, sharing, switching and interaction features in the space and time domains, the estimated maximum modal and total amplitudes, the resonant nonlinear modes of flexible cylinders and their space–time modifications, and the influence of fluid/structure parameters. A shortcoming of single-mode or linear structural model is underlined. Some quantitative and qualitative comparisons of numerical/experimental results are discussed to demonstrate the validity and required improvement of the proposed modelling and analysis predictions.
© 2010 Elsevier Ltd. All rights reserved.

Keywords: Vortex-induced vibration; Distributed wake oscillator; Flexible cylinder; Multi-mode interaction; Geometric nonlinearities; Inclined sagged cable; Tensioned beam

1. Introduction

Vortex-induced vibration (VIV) of flexible cylindrical structures such as risers, mooring cables, tethers and pipelines exhibits intriguing fluid–solid interaction phenomena in many offshore engineering applications. When exposed to current flows, these slender bodies undergo nonlinear finite-amplitude oscillations due to the space–time varying hydrodynamics associated with vortex shedding. Because VIV results in an increased mean drag and high oscillating stress-induced fatigue in long flexible structures, VIV is one of the utmost concerns in deepwater developments.

*Tel.: +44 141 548 3463; fax: +44 141 552 2879.
E-mail address: narakorn.srinil@strath.ac.uk.

Nomenclature

A, B	first-order forms in low-order model
A_f	area of displaced fluid volume
A/D	experimental maximum amplitude
A_n/D (A_R/D)	maximum modal (total) amplitudes
A_{rms}/D	root-mean-squared amplitudes
c	structural damping coefficient
C_1, C_2	coefficients in static shape analysis
C_A	added mass coefficient
C_L	fluctuating lift coefficient
C_{L0}	lift coefficient of static cylinder
D	hydrodynamic diameter
EA_r	axial stiffness
EI	bending stiffness
F, G	empirical wake coefficients
f_d	natural frequency of mode predominating in VIV
f_n, d_n	generalized displacement variables
H_1, H_2	lift force components
k	coordinate transformation parameter
L (L/D)	cylinder length (aspect ratio)
m (m_a)	cylinder mass (potential added mass)
m^*(α^*)	mass ratio (mass-damping parameter) by Williamson and co-researchers
N	number of considered modes
p_n, e_n	generalized velocity variables
Q_x, Q_y	fluid wake variables
Re	Reynolds number
s	arc-length coordinate
S_G	Skop–Griffin mass-damping parameter
St	Strouhal number of static cylinder

t	time
T (T_H)	axial (horizontal) static tension
T_a	tension at maximum sag of cable
u	horizontal or axial displacement
u_{nm} (v_{nm})	normalized nonlinear modes
U_r	reduced flow velocity parameter
v	vertical or transverse displacement
V	current velocity
W_E	structural effective weight
x	horizontal or axial coordinate
x^*	normalized x/D, 1 being maximum
X_H (Y_H)	horizontal offset (water depth)
y	vertical or transverse coordinate
α, β, δ	mechanical parameters
γ	stall parameter
Δ	tensioned-beam parameter
δ_A, X_A, Ψ_A	variables in deriving formulae for wake coefficients
ε (σ)	Cauchy bending strain (stress)
θ (θ_r)	local (global chord) inclination angle
Λ_{nij} (Γ_{nijk})	quadratic (cubic) nonlinear coefficients in cylinder equations
μ	Skop–Griffin mass ratio
ξ	modal damping
Π_{ni} ($\Re_{nijk}$)	linear (cubic nonlinear) coefficients in wake equations
ρ	fluid density
ϕ	horizontal (axial) modal shape
φ	vertical (transverse) modal shape
ω_s	vortex shedding frequency
$\omega_{s,A}$	vortex frequency at maximum A/D
ω_n (ω_{osc})	natural (oscillating) modal frequency

In general, the VIV fatigue accumulation depends on a number of mechanical, physical and fluid–solid parameters. In essence, it is a function of structural vibration characteristics including natural frequencies, modes, amplitudes and curvatures. Depending on the relationship between vortex-shedding and natural frequencies, different modes can be concurrently or non-concurrently excited in a distributed-parameter or infinite-dimensional system. These entail an intrinsic feature of multi-mode interactions in the coupled fluid–structure system. To examine a variety of dynamic scenarios caused by the hydrodynamics and structural geometric nonlinearities, a computationally robust model and systematic approach to the VIV of flexible structures with different curved/straight configurations is needed.

Many studies have attempted to numerically investigate VIV of rigid and flexible cylinders (Gabbai and Benaroya, 2005; Sarpkaya, 2004; Williamson and Govardhan, 2004). For flexible cylinders, the VIV predictions are accomplished by employing either computational fluid dynamics (CFD) or a semi-empirical approach (Chaplin et al., 2005a; Larsen and Halse, 1997). The main difference between these two approaches is the modelling of the hydrodynamics. Usually, the CFD-based procedure solves the Navier–Stokes equations to obtain the time-dependent fluid forces in two-dimensional planes which are, in turn, integrated into a finite-element structural model (Willden and Graham, 2003). This method, albeit convincingly capturing the fluid physics, requires a large amount of data storage and computational effort in numerical simulations in order to handle multi-degree-of-freedom motions of long flexible structures and a series of parametric studies with varying parameters. Owing to the limited computer technology at the present time, the CFD-based approach is not yet a practical solution to actual analysis and design involving a large number of variables. Consequently, several exiting commercial codes still rely upon a semi-empirical approach in which the accuracy of VIV response prediction is strongly related to experimental data applicable to the modelling conditions. Based on a recent comparison of several numerical tools, Chaplin et al. (2005a) showed that the semi-empirical approach is more successful than the CFD-based approach in evaluating the VIV response of a vertical straight beam in a stepped current.

With regard to the semi-empirical approach, various low-order fluid models have been proposed in the literature and the so-called nonlinear wake oscillators are perhaps the simplest low-computational models (Gabbai and Benaroya, 2005). Being phenomenological, a wake oscillator is generally based on a van der Pol equation which captures such fundamental VIV phenomena as lock-in and self-limiting amplitudes. As regards the wake characterization, an attempt to derive the wake oscillator from the fluid mechanics of vortex shedding street has been presented and discussed by Iwan and Blevins (1974). Nevertheless, some assumptions are kept in mind when utilizing the wake oscillator. These comprise, for instance, the consideration of nominal two-dimensional flow, the full correlation length of vortex shedding along the length of flexible cylinder during the lock-in and the omitted effect of end boundaries on flow behaviour. Since the pioneering idea of Bishop and Hassan (1964) and the subsequent work of Hartlen and Currie (1970), many wake oscillator models have been introduced and modified mostly to approximate the unsteady lift fluid forces acting on rigid cylinders in uniform flows (Gabbai and Benaroya, 2005). Recently, refined wake oscillators are given by Skop and Balasubramanian (1997) and Facchinetti et al. (2004). New models overcome a limitation of older models in view of evaluating the self-limiting response at zero structural damping. They also have successfully been applied to VIV analyses of flexible cylinders such as a horizontally suspended cable (Kim and Perkins, 2002) and a catenary-shaped riser (Srinil et al., 2009) based on a single modal expansion analysis, and vertical tensioned beam (Violette et al., 2007) based on a finite difference discretization.

In spite of previous extensive investigations, insights into nonlinear multi-mode dynamics of long flexible structures undergoing VIV, even in uniform flow cases, are lacking. With reference to recent large-scale or *in situ* experimental observations, some interesting aspects comprise the space/time sharing, switching and interaction of multiple modes in different lock-in or synchronization regimes along with the estimation of response amplitudes (Chaplin et al., 2005b; Jaiswal and Vandiver, 2007; Trim et al., 2005), the dependence of VIV on Reynolds number (Swithenbank et al., 2008), the influence of cylinder initial curvatures resulting in modal interactions (Hover et al., 1997a, 1997b) and the highly modulated responses (Chaplin et al., 2005b; Chasparis et al., 2009). These aspects will be discussed in this paper based on a low-order multi-mode model and numerical approach. Recently, Violette et al. (2010) have performed a linear stability approach to identify the mode switching with varying flow velocity and the time sharing of two excited modes in VIV of a straight cable. Nevertheless, owing to the employed linearized structural and wake oscillator models, the estimation of maximum amplitudes and the effect of geometric/wake nonlinearities in both space and time were disregarded in their studies. These issues will be accounted for and discussed herein.

This paper presents a general low-order fluid–solid interaction model capable of evaluating the nonlinear multi-mode dynamics and interactions of flexible curved/straight structures undergoing VIV. Cross-flow motions due to distributed lift forces of inclined sagged cables and tensioned beams are investigated. The paper is organized as follows. In Section 2, the nonlinear equations of structural motions based on a flexural curved cable model and the empirical hydrodynamic model based on a modified wake oscillator are summarized. A low-order multi-mode wake/cylinder interaction model is then developed in Section 3, along with a discussion on wake coefficients. Based on numerical investigations, several features are highlighted in Section 4, including the modal characteristics of curved/straight structures (Section 4.1), the nonlinear time histories of the cylinder/fluid wake (Section 4.2), the response amplitude diagrams (Section 4.3), the resonant nonlinear modes of flexible cylinder (Section 4.4), the influence of Reynolds number (Section 4.5) and the role of geometric nonlinearities (Section 4.6). Some numerical/experimental comparisons are discussed (Section 4.7), along with some aspects on VIV modelling and predictions (Section 4.8). The paper ends with a summary and concluding remark in Section 5.

2. Nonlinear structural and hydrodynamic models

A great majority of research literature dealing with VIV modelling and analysis of flexible cylinders considers a linear equation governing the transverse motion of straight tensioned beams or cables. This model is limited from a practical viewpoint since there are different kinds of curved structures in actual applications. In addition, the effect of geometric nonlinearities (i.e. structural nonlinear stiffness) on VIV of long flexible cylinders may be considerable depending on the system parameters, vibration amplitudes and multi-mode interactions. To fully capture both the effects of varying initial curvatures and geometric nonlinearities, a general nonlinear fluid/structure model – valid for both inclined curved and straight cylindrical structures – is considered.

With reference to a fixed Cartesian coordinate system, Fig. 1(a) (1(b)) displays a fully submerged inclined sagged cable (vertical tensioned beam) model having an equilibrium length L and being connected from a stationary floating structure to the seafloor with pinned–pinned supports. The incoming flow is considered to be spatially uniform and aligned with the Z-direction (see also a remark in Section 4.8). In Fig. 1(a), XY denotes the plane of initial static equilibrium and cross-flow motions of cable, with horizontal offset X_H and water depth Y_H defining a global chord inclination angle as $\theta_r = \tan^{-1}(Y_H/X_H)$.
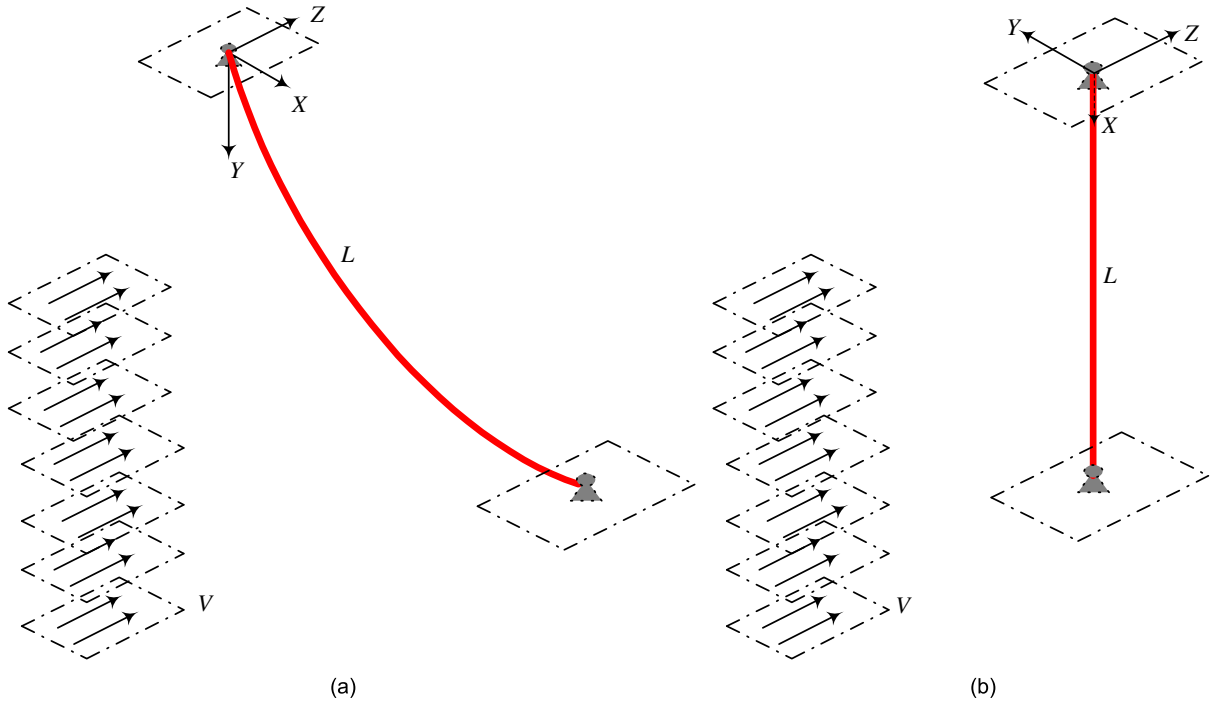
Fig. 1. A model of flexible (a) curved and (b) straight cylindrical structures in uniform currents.

Based on finite-amplitude vibrations, the geometrically nonlinear partial-differential equations describing cross-flow motions about the static configuration of a flexural inclined curved cable in water are expressed in a general dimensional form as (Srinil et al., 2007, 2009)

$$(m + m_a)\frac{\partial^2 u}{\partial t^2} + c\frac{\partial u}{\partial t} = \frac{\partial}{\partial s}\left\{ T\left(\frac{\partial u}{\partial s}\right) + EA_r\left(\frac{\partial x}{\partial s}\frac{\partial u}{\partial s} + \frac{\partial y}{\partial s}\frac{\partial v}{\partial s} + \frac{1}{2}\left(\left(\frac{\partial u}{\partial s}\right)^2 + \left(\frac{\partial v}{\partial s}\right)^2\right)\right)\left(\frac{\partial x}{\partial s} + \frac{\partial u}{\partial s}\right) - EI\frac{\partial}{\partial s}\left(\frac{\partial^2 u}{\partial s^2}\right)\right\} + H_1,$$

(1)

$$(m + m_a)\frac{\partial^2 v}{\partial t^2} + c\frac{\partial v}{\partial t} = \frac{\partial}{\partial s}\left\{ T\left(\frac{\partial v}{\partial s}\right) + EA_r\left(\frac{\partial x}{\partial s}\frac{\partial u}{\partial s} + \frac{\partial y}{\partial s}\frac{\partial v}{\partial s} + \frac{1}{2}\left(\left(\frac{\partial u}{\partial s}\right)^2 + \left(\frac{\partial v}{\partial s}\right)^2\right)\right)\left(\frac{\partial y}{\partial s} + \frac{\partial v}{\partial s}\right) - EI\frac{\partial}{\partial s}\left(\frac{\partial^2 v}{\partial s^2}\right)\right\} + H_2,$$

(2)

in which s denotes arc-length coordinate and t denotes time, x and y are the static coordinates with u and v being the associated dynamic displacements in the horizontal (X) and vertical (Y) directions, respectively. The flexible cylinder properties, including the mass (m), viscous damping (c), bending (EI) and axial (EA_r) stiffness, are assumed to be spatially uniform. The fluid properties comprise potential added mass ($m_a = C_A \rho A_f$), density (ρ), cross-sectional area of displaced volume (A_f) and added mass coefficient (C_A). T denotes the varying axial tension while H_1 and H_2 represent the components of space–time varying lift forces leading to cross-flow VIV. Note that the effects of shear, torsion, seabed interaction, surface waves, support movement, tangential drag forces and in-line VIV in the Z-direction are herein neglected. Moreover, the $EI(\partial^4 x/\partial s^4)$ and $EI(\partial^4 y/\partial s^4)$ terms governing the bending effect on a static curved configuration are omitted from Eq. (1) and Eq. (2), respectively, in order to arrive at a closed-form formula for a catenary cable (see Eq. (6)). A complete three-dimensional equations of structural motion subject to both cross-flow/ in-line VIV can be found in Srinil et al. (2009).

For convenience in the low-order modelling which relies on continuous functions of curved static profiles and linear modal shapes, the s coordinate is projected onto the horizontal x coordinate through the transformation

$$\frac{\partial x}{\partial s} = \frac{1}{(1 + y'^2)^{1/2}} = \frac{1}{k},$$

(3)

where a prime denotes differentiation with respect to x which is now utilized as a new independent variable. By substituting Eq. (3) into Eqs. (1) and (2) and normalizing all the displacement-related variables/derivatives with respect to the hydrodynamic diameter (D), the geometrically nonlinear equations of cross-flow motions of an inclined cable become

$$k\ddot{u} + k\frac{c}{m+m_a}\dot{u} + \delta\left(\frac{1}{k^3}u'''\right)' - \beta\left\{u' + \frac{\alpha}{k^3}(u' + y'v') + \frac{\alpha}{k^3}\left(u'^2 + y'u'v' + \frac{1}{2}(u'^2 + v'^2)\right) + \frac{\alpha}{2k^3}(u'^3 + u'v'^2)\right\}'$$
$$= \frac{H_1 k}{(m+m_a)D}, \tag{4}$$

$$k\ddot{v} + k\frac{c}{m+m_a}\dot{v} + \delta\left(\frac{1}{k^3}v'''\right)' - \beta\left\{v' + \frac{\alpha}{k^3}(y'u' + y'^2v') + \frac{\alpha}{k^3}\left(u'v' + y'v'^2 + \frac{y'}{2}(u'^2 + v'^2)\right) + \frac{\alpha}{2k^3}(u'^2v' + v'^3)\right\}'$$
$$= \frac{H_2 k}{(m+m_a)D}, \tag{5}$$

where overdot denotes differentiation with respect to t. The mechanical parameters are $\delta = EI/(m+m_a)D^4$, $\beta = T_H/(m+m_a)D^2$, $\alpha = EA_r/T_H$, with $T_H = T/k$ being a constant horizontal component of cable tension. By assuming that a planar static configuration of cable is only due to its effective weight (W_E) accounting for the buoyancy force, an exact closed-form hyperbolic function describing $y = y(x)$ reads

$$y(x) = \frac{-T_H}{W_E D}\cosh\left(\frac{W_E D}{T_H}x + C_1\right) + C_2, \tag{6}$$

where C_1 and C_2 are determined based on boundary conditions. By using the cosine law, the horizontal and vertical components (H_1, H_2) of normal lift force (C_L) in Eqs. (4) and (5) are given by

$$H_1 = -\frac{1}{2}\rho DV^2 C_L \sin\theta = \frac{1}{2}\rho DV^2 C_{Lx}, \tag{7}$$

$$H_2 = \frac{1}{2}\rho DV^2 C_L \cos\theta = \frac{1}{2}\rho DV^2 C_{Ly}, \tag{8}$$

in which V is the flow velocity, the associated lift coefficients $C_{Lx} = Q_x - 2\gamma\dot{u}\,/\omega_s$ and $C_{Ly} = Q_y - 2\gamma\dot{v}\,/\omega_s$ (Srinil et al., 2009), γ the so-called stall parameter (Skop and Balasubramanian, 1997), ω_s the vortex-shedding frequency (rad/s) with $\omega_s = 2\pi \mathrm{St}V/D$ (Sumer and Fredsøe, 2006), St the Strouhal number and θ the cable local inclination angle measured clockwise from the X-axis. The assumed variables Q_x and Q_y are governed by the following companion distributed wake oscillators (Srinil et al., 2009):

$$\frac{\ddot{Q}_x}{\sin\theta} - \frac{\omega_s G C_{L0}^2 \dot{Q}_x}{\sin\theta} + \frac{4\omega_s G Q_x^2 \dot{Q}_x}{\sin^3\theta} + \frac{\omega_s^2 Q_x}{\sin\theta} = \frac{\omega_s F\dot{u}}{\sin\theta}, \tag{9}$$

$$\frac{\ddot{Q}_y}{\cos\theta} - \frac{\omega_s G C_{L0}^2 \dot{Q}_y}{\cos\theta} + \frac{4\omega_s G Q_y^2 \dot{Q}_y}{\cos^3\theta} + \frac{\omega_s^2 Q_y}{\cos\theta} = \frac{\omega_s F\dot{v}}{\cos\theta}, \tag{10}$$

where C_{L0} is the lift coefficient of a stationary cylinder, F and G are the two variable empirical wake coefficients which depend on system parameters (see Section 3). It is worth noting that Eqs. (9) and (10) resemble the original wake oscillator of Skop and Balasubramanian (1997), with the space-dependent ($\sin\theta$, $\cos\theta$) terms being incorporated into the former in an attempt to capture both the effect of varying initial curvatures on the wake and the concurrent horizontal/vertical dynamics of cable through Eqs. (4) and (5).

Note that, at a discrete x position, the local inclination angle $\theta(x)$ is arbitrary since $\theta \approx \tan^{-1}(y')$. Depending on an inclined curved static configuration (Eq. (6)), the spatial gradient $y'(x)$ may be positive, negative or even zero (i.e. at cable maximum sag). Accordingly, a mathematical singularity occurs in Eq. (9) or (10) when θ becomes, e.g., $0°$ or $90°$, respectively. Nevertheless, it will be shown in Section 3 that such singularity can be overcome through the Galerkin-based procedure whereby the continuous $\theta(x)$ function based on Eq. (6) is incorporated into the ensuing integrals involving modal shape functions (see Eqs. (17) and (20)).

There has also been a discussion in the literature on the choice of coupling term (structural displacement, velocity and acceleration) in the wake oscillator (i.e. the right term in Eq. (9) or (10)). Based on some comparisons with experimental results of rigid cylinders, Facchinetti et al. (2004) recommended the acceleration coupling model. However, this model has recently been commented by Farshidianfar and Zanganeh (2010) who showed, on the other hand, the superior results of the velocity coupling model. Hence, the velocity coupling term is herein chosen by considering and modifying

the Skop and Balasubramanian's model. Other modifications of the Skop–Balasubramanian wake oscillator can be found in the paper of Kim and Perkins (2002) where some additional nonlinear terms have been included to account for the coupling of lift/drag forces, and in the work of Balasubramanian et al. (2000) where a diffusion term has been included to account for a cellular vortex shedding in sheared flows.

Eqs. (1)–(10) are considered for arbitrarily inclined cables. In the case of uniform-tension beam whose coordinate system is shown in Fig. 1(b), the condition $\partial s \approx \partial x$ is applied to Eqs. (4) and (5) with $y' = 0$ ($k = 1$), $H_1 = 0$ and $T_H = T$. Thus, u and v in the reduced Eqs. (4) and (5) describe axial and transverse motions of straight tensioned beam, respectively. In turn, only Eq. (10) with $\cos \theta = 1$ is considered for the lift force. Overall, Eqs. (4) and (5) account for the longitudinal inertia effect and quadratic/cubic nonlinear terms due to the dynamic extensibility, even in the absence of initial curvatures (Srinil et al., 2007). Many VIV studies have neglected the geometric nonlinearities. Yet, as recently remarked by Bearman (2009), their potential effects might be considerable and cannot be ruled out. They will be highlighted in Sections 4.6 and 4.7 based on a comparison of linear versus nonlinear cylinder models.

3. Low-order multi-mode wake/cylinder interaction model

We aim to numerically investigate multi-mode VIV responses of curved/straight structures through a systematic low-order model. This computationally robust model is practically useful when dealing with large parametric studies. Due to the commensurability of vortex-shedding and natural frequencies, certain modes may take part in the coupled fluid–structure system, even in the case of uniform flow with a single velocity (Chaplin et al., 2005b; Willden and Graham, 2003). Because some recently observed VIV of full-scale drilling pipes tends towards standing wave responses with increasing amplitudes (Tognarelli et al., 2008), standing wave characteristics are herein assumed. The travelling wave responses would become more relevant at higher-order modes and/or in sheared flow cases (Vandiver et al., 2009). In fact, the travelling wave behaviour is the expected response of slender structures with high aspect ratios (Lie and Kaasen, 2006).

By rearranging Eqs. (4), (5), (9) and (10) in their first-order forms (A, B) and assuming that the wake oscillates modally and concurrently with the cylinder, both cylinder and wake variables are postulated in terms of a full eigenbasis by letting

$$\dot{u} = A_1 \rightarrow \quad u(x,t) = \sum_{n=1}^{\infty} \phi_n(x) f_n(t), \quad A_1(x,t) = \sum_{n=1}^{\infty} \phi_n(x) p_n(t),$$

$$\dot{v} = A_2 \rightarrow \quad v(x,t) = \sum_{n=1}^{\infty} \varphi_n(x) f_n(t), \quad A_2(x,t) = \sum_{n=1}^{\infty} \varphi_n(x) p_n(t), \tag{11}$$

$$\dot{Q}_x = B_1 \rightarrow \quad Q_x(x,t) = \sum_{n=1}^{\infty} \phi_n(x) d_n(t), \quad B_1(x,t) = \sum_{n=1}^{\infty} \phi_n(x) e_n(t),$$

$$\dot{Q}_y = B_2 \rightarrow \quad Q_y(x,t) = \sum_{n=1}^{\infty} \varphi_n(x) d_n(t), \quad B_2(x,t) = \sum_{n=1}^{\infty} \varphi_n(x) e_n(t), \tag{12}$$

where ϕ_n and φ_n are synchronized horizontal (axial) and vertical (transverse) displacement shape functions of nth cable (beam) modes, respectively. These eigenfunctions have been obtained based on a Fourier sine-based series in conjunction with a hybrid analytical–numerical eigensolution of linear equations of free undamped motions in Eqs. (4) and (5) (Srinil et al., 2007, 2009). In Eq. (11) ((12)), f_n (d_n) and p_n (e_n) denote, respectively, the generalized displacement and velocity of the cylinder (wake). By substituting Eqs. (11) and (12), into (4), (5), (9) and (10), applying the Galerkin procedure with pinned–pinned boundary conditions and orthonormalization of modes, and assuming the lock-in condition ($\omega_s \approx \omega_n$) through Eqs. (7) and (8), a low-order model describing the multi-mode interaction in the VIV of a coupled cylinder/wake system is given by the following nonlinear ordinary-differential equations:

$$\dot{f}_n = p_n, \tag{13}$$

$$\dot{p}_n = -2\mu S_G \omega_n p_n - \omega_n^2 f_n + \mu \omega_n^2 (d_n - 2\gamma p_n / \omega_s) + \sum_{i=1}^{\infty} \sum_{j=1}^{\infty} \Lambda_{nij} f_i f_j + \sum_{i=1}^{\infty} \sum_{j=1}^{\infty} \sum_{k=1}^{\infty} \Gamma_{nijk} f_i f_j f_k, \tag{14}$$

$$\dot{d}_n = e_n, \tag{15}$$

$$\dot{e}_n = \omega_s G C_{L0}^2 e_n - \omega_s^2 d_n + \omega_s F p_n + \sum_{\substack{i=1,\\i\neq n}}^{\infty} \Pi_{ni}(\omega_s G C_{L0}^2 e_i - \omega_s^2 d_i + \omega_s F p_i) - 4\omega_s G \sum_{i=1}^{\infty}\sum_{j=1}^{\infty}\sum_{k=1}^{\infty} \Re_{nijk} d_i d_j e_k, \tag{16}$$

where ω_n are the natural frequencies in still water, S_G the mass-damping or so-called Skop–Griffin parameter with $S_G = \xi/\mu$ (Skop and Balasubramanian, 1997), μ the fluid-to-cylinder mass ratio with $\mu = \rho D^2/8\pi^2 St^2(m + m_a)$, and ξ the modal damping. In the above system, ξ and thus S_G (as well as F and G) are assumed to be mode-independent. Overall, the linear (Π_{ni}), quadratic (Λ_{nij}) and cubic (Γ_{nijk}, $\Re_{nijk}$) nonlinear coefficients – which govern the multi-mode contributions and interaction effects – are given, respectively, by

$$\Pi_{ni} = \int_0^{X_H/D} k\left(\frac{\phi_n\phi_i}{y'} + \varphi_n\varphi_i\right)dx \bigg/ \int_0^{X_H/D} k\left(\frac{\phi_n^2}{y'} + \varphi_n^2\right)dx, \tag{17}$$

$$\Lambda_{nij} = -\beta\alpha \int_0^{X_H/D} \frac{1}{k^3}\left(\frac{3}{2}\phi_n'\phi_i'\phi_j' + y'\phi_n'\phi_i'\varphi_j' + \frac{1}{2}\phi_n'\varphi_i'\varphi_j' + \varphi_n'\phi_i'\varphi_j' + \frac{y'}{2}\varphi_n'\phi_i'\phi_j' + \frac{3}{2}y'\varphi_n'\varphi_i'\varphi_j'\right)dx, \tag{18}$$

$$\Gamma_{nijk} = -\frac{\beta\alpha}{2} \int_0^{X_H/D} \frac{1}{k^3}(\phi_n'\phi_i'\phi_j'\phi_k' + \phi_n'\phi_i'\varphi_j'\varphi_k' + \varphi_n'\phi_i'\phi_j'\varphi_k' + \varphi_n'\varphi_i'\varphi_j'\varphi_k')dx, \tag{19}$$

$$\Re_{nijk} = \int_0^{X_H/D} k^3\left(\frac{\phi_n\phi_i\phi_j\phi_k}{y'^3} + \varphi_n\varphi_i\varphi_j\varphi_k\right)dx \bigg/ \int_0^{X_H/D} k\left(\frac{\phi_n^2}{y'} + \varphi_n^2\right)dx. \tag{20}$$

Depending on a number of considered modes N, the total N linear and N^2 (N^3) nonlinear quadratic (cubic) coefficients in each modal equation can be calculated *a priori*, by numerically integrating Eqs. (17)–(20) with 64-point Gaussian Quadrature. In the case of straight beams, X_H/D becomes L/D. Eq. (16) results in N coupled van der Pol oscillators having a unique vortex-shedding frequency ω_s, which, in turn, interacts with different cylinder frequencies ω_n in Eq. (14). This accounts for an inherent detuning of system frequencies during VIV. For given initial displacement/velocity conditions (f_n, p_n, d_n, e_n), the $4N$ nonlinear equations are simultaneously solved by direct numerical integrations with a sufficiently small time step (Srinil and Rega, 2008b). Overall, the coupled wake/cylinder system depends on the input parameters (δ, β, α, ξ, μ, S_G), the curved static configuration profile $y(x)$, modal shape functions and characteristics (ω_n, ϕ_n, φ_n), strength of geometric/wake nonlinearities (Eqs. (18)–(20)) and the empirical parameters (St, C_{L0}, γ, F, G).

As regards the wake coefficients, F and G may be derived as functions of system parameters defining both the flow and cylinder properties in the experiments. Typically, cross-flow VIV of spring-mounted rigid cylinders in uniform flows have been tested, and the associated steady-state solutions of coupled linear (cylinder) and nonlinear (wake) oscillators are determined. These entail a relationship of wake coefficients to fluid-cylinder parameters and measured responses. Following Skop and Balasubramanian (1997), F and G depend on the measured maximum amplitude A/D of cylinder and frequency ratio $\omega_{s,A}/\omega_n$ with $\omega_{s,A}$ being the vortex frequency at maximum A/D. Some relevant formulae are summarized as follows. In Eq. (16), the velocity coupling (p_n) terms are dependent on F which reads

$$F = \frac{\mu(S_G + \gamma)^2}{2}(\delta_A^2 + 4)(\Psi_A - \delta_A), \tag{21}$$

whereas the wake damping terms depend on G given by

$$G = \frac{F}{2C_{L0}^2(S_G + \gamma)}\frac{3\delta_A^2 - 4}{\delta_A(\delta_A^2 + 4)}, \tag{22}$$

in which

$$\delta_A = -\left\{\frac{-(8X_A - 1) + \sqrt{(8X_A - 1)^2 + 48X_A(4X_A - 1)}}{6X_A}\right\}^{1/2}, \tag{23}$$

$$X_A = \left\{\frac{(S_G + \gamma)(A/D)}{C_{L0}}\right\}^2, \tag{24}$$

$$\boldsymbol{\Psi}_A = \frac{2}{\mu(\mathrm{S_G} + \gamma)}\left[\frac{\omega_{s,A}}{\omega_n} - 1\right]. \tag{25}$$

Apart from the explicit (implicit) empirical parameters C_{L0} and γ (St) in the above expressions, A/D and $\omega_{s,A}/\omega_n$ are described by the following $\mathrm{S_G}$-based functions (Skop and Balasubramanian, 1997)

$$\frac{A}{D} = \frac{0.385}{(0.12 + \mathrm{S_G^2})^{1/2}}, \tag{26}$$

$$\frac{\omega_{s,A}}{\omega_n} = 1.216 + \frac{0.084}{1 + 2.66\mathrm{S_G^2}}. \tag{27}$$

These analytical expressions (Eqs. (21)–(27)) reveal the highly nonlinear relationships between wake coefficients and system parameters. One may examine *a priori* the influence of individual parameter on coefficients F and G through a graphical plot. As exemplified by Srinil et al. (2009), $F(G)$ nonlinearly increases (decreases) as $\mathrm{S_G}$ increases with decreasing μ while keeping ξ and other parameters constant. In previous studies based on a single-mode cross-flow VIV (Kim and Perkins, 2002; Srinil et al., 2009), F and G were kept constant when parametrically varying V; thus, the influence of Re was neglected. To further account for the Re effect in the VIV prediction model, a recent empirical formula given by Govardhan and Williamson (2006) is considered in place of Eq. (26). The relevant equation reads

$$\frac{A}{D} = (1 - 1.12\alpha^* + 0.30\alpha^{*2})\log(0.41\,\mathrm{Re}^{0.36}), \tag{28}$$

in which the mass-damping parameter is $\alpha^* = (m^* + C_A)\xi$ and the cylinder-to-fluid mass ratio is $m^* = m/(\pi\rho D^2/4)$, which are defined differently from $\mathrm{S_G}$ and μ (Skop and Balasubramanian, 1997), respectively. With Eq. (28), both F and G values can be recalculated when varying V. In Section 4.5, the models with fixed and varied wake coefficients (defined herein as Fixed-FG and Varied-FG models) will be considered and compared to highlight the effect of Re on multi-mode VIV predictions. It is worth emphasizing that establishing the dependence of empirical wake coefficients on system parameters is theoretically and practically useful because different cylindrical structures having different properties can be straightforwardly analyzed without demanding a new experimental setup and testing involving high costs and times. Conversely, more experimental tests are needed to calibrate the variable hydrodynamic coefficients for a more complex model involving a higher number of influencing parameters.

4. Parametric investigations and discussion

To examine the multi-mode VIV characteristics of different curved/straight structures, an inclined cable and two tensioned beams (beam$_1$ and beam$_2$) having the properties given in Table 1 are investigated based on Eqs. (13)–(16). Other constant parameters are $C_A = 1$, $C_{L0} = 0.28$ and $\gamma = 0.183$ (Skop and Balasubramanian, 1997). Note that while in principle being dependent on Re (Norberg, 2003), C_{L0} and St are kept fixed when varying V. Both the cable and beam$_1$ have the same properties (Srinil and Rega, 2007), except that $\theta_r = 30°$ for the cable. Beam$_2$ is the pipe used in an ExxonMobil experimental campaign whose post-processed data have been reported by Tognarelli et al. (2004).

Table 1
Dimensionless parameters of considered curved/straight structures.

Parameters	Cable/Beam$_1$	Beam$_2$
Δ	272	22
L/D	2581	482
μ	0.044	0.173
m^*	8.14	2.23
ξ	0.01	0.003
St	0.20	0.17
$\mathrm{S_G}$	0.227	0.017
F	0.644	0.319
G	0.489	1.887

This beam$_2$ is compared with beam$_1$ (Sections 4.5 and 4.6) and used in a comparison between numerical/experimental results (Section 4.7). While the cylinder slenderness is described by an aspect ratio (L/D), the tension versus bending contributions may be characterized by the dimensionless tensioned-beam parameter $\Delta = L\sqrt{T_a/EI}$, where T_a is a tension at maximum sag (average tension) of the cable (beam) (Srinil et al., 2009). Note that T_a is herein considered as a reference value but this may alternatively be, e.g., the maximum (minimum) tension at the top (bottom). As shown in Table 1, cable/beam$_1$ are more slender and dominated by tension than beam$_2$ since the former have greater L/D and Δ, respectively. In addition, cable/beam$_1$ have larger mass (m^*) and damping (ξ) ratios. Depending on S$_G$, the fixed F and G values of cable/beam$_1$ and beam$_2$ are different. These overall distinctions will be kept in mind when making a discussion and comparison of prediction results.

In the following, the modal characteristics of the cable/beams are first analyzed. By focusing on the VIV prediction for the curved nonlinear cable, the analyses of time histories, modal amplitudes and space–time displacement profiles are discussed in Sections 4.2, 4.3 and 4.4, respectively, based on the Fixed-FG model. To highlight the Re effect, results from Fixed- and Varied-FG models are compared in Section 4.5. The influence of geometric nonlinearities is emphasized in Section 4.6. The numerical predictions are validated by experimental results in Section 4.7. Finally, some aspects on the VIV modelling and predictions are drawn in Section 4.8.

4.1. Modal characteristics of flexible curved/straight structures

The dependence of VIV on modal characteristics distinguishes flexible cylinders from rigid cylinders, and the dependence of VIV on initial curvatures distinguishes curved cylinders from straight cylinders. Based on 20 sine series considered in the linear dynamic analysis, the natural frequencies and associated normalized modal shape functions are shown in Table 2 and Fig. 2, respectively, for the lowest 8 modes of the cable and beams. In Fig. 2, x^* indicates how the coordinate x, which has initially been non-dimensionalized by D, is further normalized such that the maximum value – being X_H/D (L/D) in the cable (beam) case – becomes unity. Consistently, this normalization is also applied to shape functions depicted in Fig. 2, with dashed and solid lines denoting horizontal (ϕ_n) and vertical (φ_n) displacement components of the cable, respectively. For straight beam$_1$ and beam$_2$, the normalized mode shapes are identical, and only transverse components (φ_n) are displayed by dotted lines since axial (ϕ_n) components appear at higher-order modes.

Fig. 2 reveals that the curved cable exhibits asymmetric mode shapes due to the effect of varying initial curvatures, whereas the straight beams exhibit typical string modes, both symmetric and anti-symmetric. These qualitative differences affect the multi-mode interaction coefficients through Eqs. (17)–(20). In fact, owing to the zero initial curvatures and/or the orthogonality properties of symmetric/anti-symmetric transverse modes (Srinil and Rega, 2007), the linear Π_{ni} (Eq. (17)) and quadratic Λ_{nij} (Eq. (18)) coefficients, and some of the cubic Γ_{nijk} and $\Re_{nijk}$ coefficients

Table 2
Natural frequencies in still water and their nearly integer frequency ratios of considered curved/straight structures.

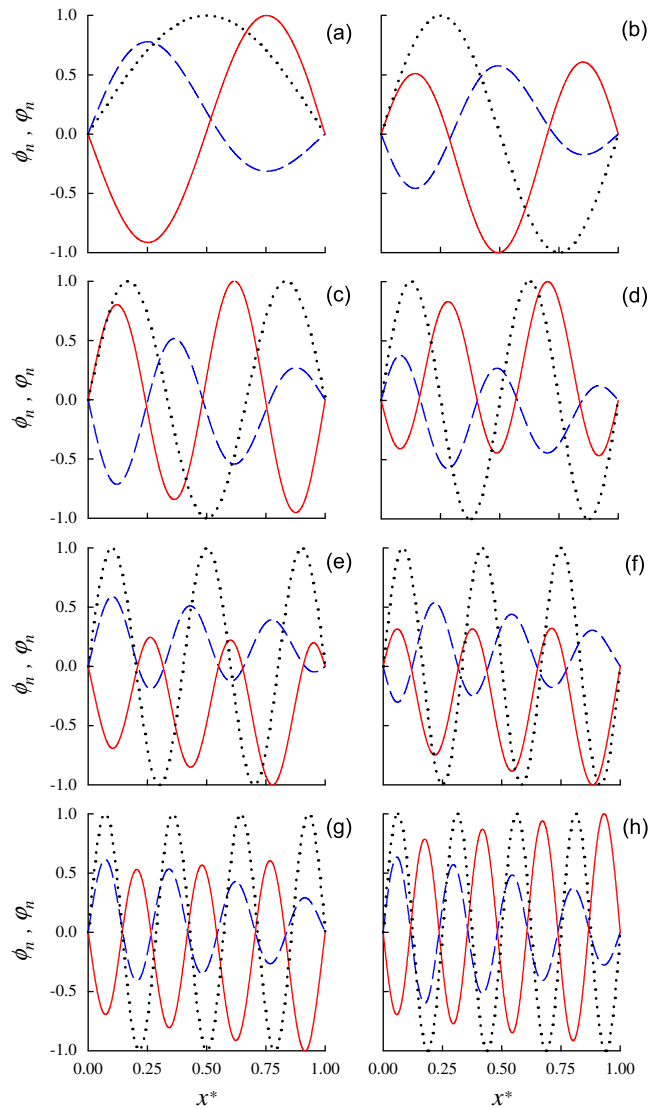| Frequency (rad/s)	Cable	Beam$_1$	Beam$_2$
ω_1	0.719	0.365	8.662
ω_2	1.033	0.730	17.840
ω_3	1.461	1.095	28.004
ω_4	1.755	1.461	39.544
ω_5	2.168	1.827	52.762
ω_6	2.229	2.194	67.883
ω_7	2.622	2.562	85.066
ω_8	2.948	2.931	104.424
Frequency ratio	**Cable**	**Beam$_1$**	**Beam$_2$**
1:1	$\omega_6{:}\omega_5$	–	–
2:1	$\omega_3{:}\omega_1$	$\omega_2{:}\omega_1$	$\omega_2{:}\omega_1$
	$\omega_5{:}\omega_2$	$\omega_4{:}\omega_2$	$\omega_7{:}\omega_4$
	$\omega_6{:}\omega_2$	$\omega_6{:}\omega_3$	$\omega_8{:}\omega_5$
	$\omega_8{:}\omega_3$	$\omega_8{:}\omega_4$	
3:1	$\omega_5{:}\omega_1$	$\omega_3{:}\omega_1$	$\omega_5{:}\omega_2$
		$\omega_6{:}\omega_2$	$\omega_7{:}\omega_3$

Fig. 2. Normalized continuous shape functions of lowest 8 modes (a–h respectively): solid (dashed) lines denote vertical (horizontal) displacements of curved cable; dotted lines denote transverse displacements of straight beam$_1$ or beam$_2$.

(Eqs. (19) and (20) with $k = 1$ and without y' terms) of beams are trivial. However, if axial modes come into play, Λ_{nij} becomes significant (Srinil and Rega, 2008a). Furthermore, one cannot rule out axial modes by considering, e.g., a linearized tensioned-beam equation. On the contrary, overall coefficients of the inclined cable are non-trivial due to the interactions of different asymmetric modes.

Because beam$_2$ is more dominated by bending than cable/beam$_1$, the natural frequencies of beam$_2$ are much higher and more widely spaced. As shown in Table 2, the differences in frequencies between the cable and beam$_1$ are relatively small due to a small inclination of cable whereas those between beam$_1$ and beam$_2$ are considerable, being by an order or even two orders of magnitude. Overall, some of the frequencies are commensurable as nearly integer ratios. For instance, the $\omega_6{:}\omega_5$ ($\omega_5{:}\omega_2$ and $\omega_6{:}\omega_2$) ratio is about 1:1 (2:1) for the cable, whereas the $\omega_6{:}\omega_2$ ($\omega_7{:}\omega_3$) ratio is about 3:1 for beam$_1$ (beam$_2$). These sample frequency (1:1, 2:1, 3:1) ratios (see Table 2), together with the associated geometric nonlinearities, would lead to a so-called internal or auto-parametric resonance condition (Nayfeh, 2000), which, in turn, adds to the complexity of VIV prediction of flexible structures. Indeed, depending on vortex-shedding frequency (ω_s), both external (ω_s versus ω_n) and internal (amongst ω_n) resonances may be simultaneously activated. This represents a precarious

dynamic scenario responsible for large-amplitude VIV responses as will be further investigated in Section 4.5. In the following, the nonlinear time histories of cylinder and fluid wake are first discussed.

4.2. Time histories of resonantly coupled cylinder/wake with mode switching

Numerical integrations of nonlinearly coupled Eqs. (13)–(16) are performed to determine the steady-state responses of the cylinder (f_n, p_n) and wake (d_n, e_n) modal coordinates, prior to evaluating relevant response amplitudes. The time simulations depend on the input parameters, the number of modes and assigned initial displacement/velocity conditions. By way of example, the inclined cable subject to $V = 0.734$ m/s ($\omega_s \approx 2.4$ rad/s) is considered and the time series of cylinder (f_n) and wake (d_n) displacements with $N = 5$ ($n = 2$–6) are displayed in Fig. 3 based on very small initial condition values from the cable static equilibrium.

As shown in Fig. 3, a beating phenomenon with continuous amplitude modulations occurs in the modal time histories of both cylinder and fluid wake. The beginning dynamics ($t < 800$ s) are governed by the 6th-mode response having steady amplitudes. As time progresses ($t > 800$ s), other modal responses grow considerably and the dominant mode switches from the 6th mode to the 4th and 5th modes ($t > 1600$ s). At this time, all modes are resonantly coupled, becoming energetic and periodically interacting amongst themselves. The 4th mode response appears to be the most stable and steady. Note also that modal responses of the cylinder prevail over those of wake during the multi-mode interactions: this may be attributed to the fact that the structure usually controls the fluid when the lock-in or synchronization takes place (Sumer and Fredsøe, 2006). The ''mode switching'' feature along the time coordinate for a specified flow velocity, as in Fig. 3, has recently been observed in the experiments of a vertical beam partially subject to uniform flow by Chaplin et al. (2005b). Therein, the dominant 8th mode switches to the 6th and 7th modes in cross-flow VIV. Violette et al. (2010) have theoretically explained this behaviour based on the linear stability approach. Because different modes can be excited at different ($t < 800$ versus $t > 1600$ s) and coincident ($t > 1600$ s) time instants, the associated concepts of ''time sharing'' (Jaiswal and Vandiver, 2007) and ''space sharing'' (Tognarelli et al., 2004) are, respectively, relevant to the time series in Fig. 3.

By performing a fast Fourier transform to the steady-state responses ($t > 2400$ s), the modal oscillating frequencies ω_{osc} of cylinder/wake are also reported in Fig. 3. These should be compared with ω_n in Table 2 and $\omega_s = 2.4$ rad/s based on the Strouhal law. It is evident that the coupled cylinder–wake responses of each vibration mode have the same ω_{osc}.
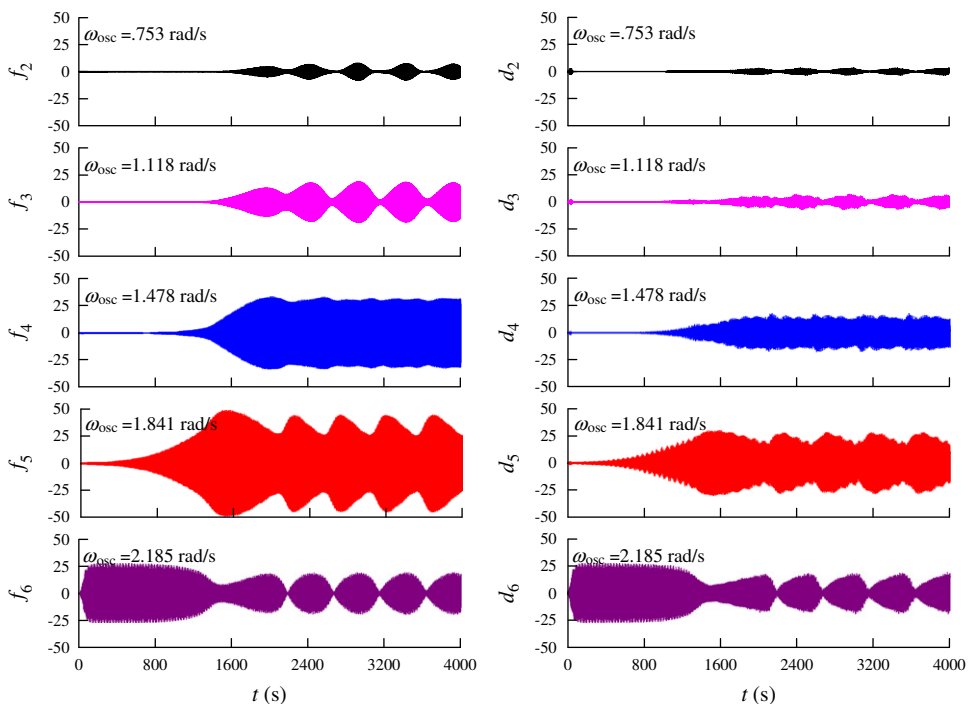

Fig. 3. Nonlinear time histories and associated oscillating frequencies of cylinder (f_n) and wake (d_n) multi-mode coordinates of curved nonlinear cable with $N = 5$ ($n = 2$–6), $V = 0.734$ m/s and small initial displacement/velocity conditions.

This highlights how multi-mode lock-in occurs, with wake modal frequencies locking onto cylinder modal frequencies, and qualitatively confirms what has been experimentally observed by Hover et al. (1997a) for inclined cables subject to flows perpendicular to the equilibrium plane. Overall, the computed ω_{osc} values (0.753, 1.118, 1.478, 1.841, 2.185 rad/s) in Fig. 3 are less than the associated ω_n (1.033, 1.461, 1.755, 2.168, 2.228 rad/s) due to the effect of varying added mass during VIV (Sumer and Fredsøe, 2006). The frequency ratios ω_{osc}/ω_n of all five modes are less than 1, decreasing consecutively from 0.98, 0.85, 0.84, 0.77 to 0.73 as the mode number increases. This further highlights how, in addition to the mass/damping parameter (Williamson and Govardhan, 2004), the hydrodynamic added mass is also mode-dependent for a flexible cylinder.

Based on other numerical simulations, it has been found that the mode switching, space/time sharing characteristics for a given flexible cylinder and V depend on both the number of interacting modes and the assigned initial conditions. The latter, in turn, affect the onset of limit cycles or steady-state responses and, of course, the computational time. To conduct a series of parametric studies with varying V, it is necessary to assign the initial conditions based on the maximum or steady-state modal responses obtained from the previous V case. In the following section, the response amplitude diagrams of flexible cylinder are discussed.

4.3. Response amplitude diagrams of flexible cylinder

It is now of interest to estimate the maximum modal and total (superimposed) amplitudes of the flexible curved cylinder, and also varying flow velocity (V) and considering different low-order (N) models. As remarked by Williamson and Govardhan (2004), one of the fundamental questions deals with the maximum attainable amplitudes of cylinders subject to VIV. In this study, the maximum amplitudes based on each *individual* mode (A_n/D) and all *superimposed* modes (A_R/D) are both evaluated. Note that the A_n/D are useful in the analysis of multi-mode contributions and interactions, as well as the determination of dominant mode(s) in VIV. On the other hand, A_R/D is useful in evaluating the total response which is in turn meaningful for the ensuing stress and fatigue analyses.

The A_n/D of the flexible cylinder are approximated by

$$A_n/D = \sqrt{[f_{n,\max}\phi_{n,\max}]^2 + [f_{n,\max}\varphi_{n,\max}]^2}, \tag{29}$$

where for the nth vibration mode, $f_{n,\max}$ is the maximum value of f_n obtained from the steady-state time histories (e.g. Fig.3 for $t > 2400$ s), and $\phi_{n,\max}$ ($\varphi_{n,\max}$) is the spatially maximum horizontal or axial (vertical or transverse) displacement of the mode shape functions of the cable or beam, respectively. Depending on the number of modes considered $N = (N_2 - N_1) + 1$, the space–time (i, j) varying displacement profiles accounting for *all* modal contributions are expressed as

$$u(x_i, t_j) = \sum_{n=N_1}^{N_2} f_n(t_j)\phi_n(x_i), \quad v(x_i, t_j) = \sum_{n=N_1}^{N_2} f_n(t_j)\varphi_n(x_i). \tag{30}$$

Accordingly, A_R/D are determined based on the spatially and temporally maximum values of $\sqrt{u^2 + v^2}$. In some cases, the root-mean-squared (rms) amplitude at a specific cylinder position $A_{\mathrm{rms}}(x_i)/D$ and the overall spatially maximum value $A_{\mathrm{rms,max}}/D$ are computed through Eq. (30), by accounting for a standard deviation in $f_n(t_j)$.

By way of example, the inclined cable is again considered with $0.1 < V < 1$ m/s. Fig. 4(a) and (b) depict the A_n/D diagrams obtained by the single-mode ($N = 1$, where $n = 1, 2, \ldots, 7$) and multi-mode ($N = 7$, $n = 1$–7) models, respectively. Note that results from 7 single-mode analyses are jointly plotted in Fig. 4(a), in contrast to results from one multi-mode analysis plotted in Fig. 4(b). As shown in Fig. 4, both quantitative and qualitative differences take place in between single-mode (Fig. 4(a)) and multi-mode (Fig. 4(b)) models, even though all seven modes are consecutively excited as V increases. In particular, the single-mode model overestimates A_n/D with a maximum value reaching 2.32 corresponding to either the 4th or 5th mode (Fig. 4(a)). This is different from the multi-mode model where the maximum A_n/D is about 1.44 corresponding to the 6th mode (Fig. 4(b)). Moreover, the single-mode model widens all modal lock-in ranges, resulting in a large overlapping area of modal amplitudes. A hysteresis effect, where the modal response reaches its peak and suddenly jumps down prior to switching to a new modal response as V increases, is captured by the multi-mode model (see, e.g., A_1/D, A_2/D and A_6/D). In accordance with Fig. 3, three dominant modes (A_4/D, A_5/D and A_6/D) appear at $V \approx 0.73$ m/s and the multi-mode lock-in involving two or three modes occurs over a particular V range in Fig. 4(b). The 5th and 6th modal responses are strongly coupled since their natural frequencies (2.168 and 2.228 rad/s) are nearly 1:1 resonant (Table 2). The coupling in VIV of two cable modes having nearly identical frequencies has been experimentally discussed by Hover et al. (1997a).
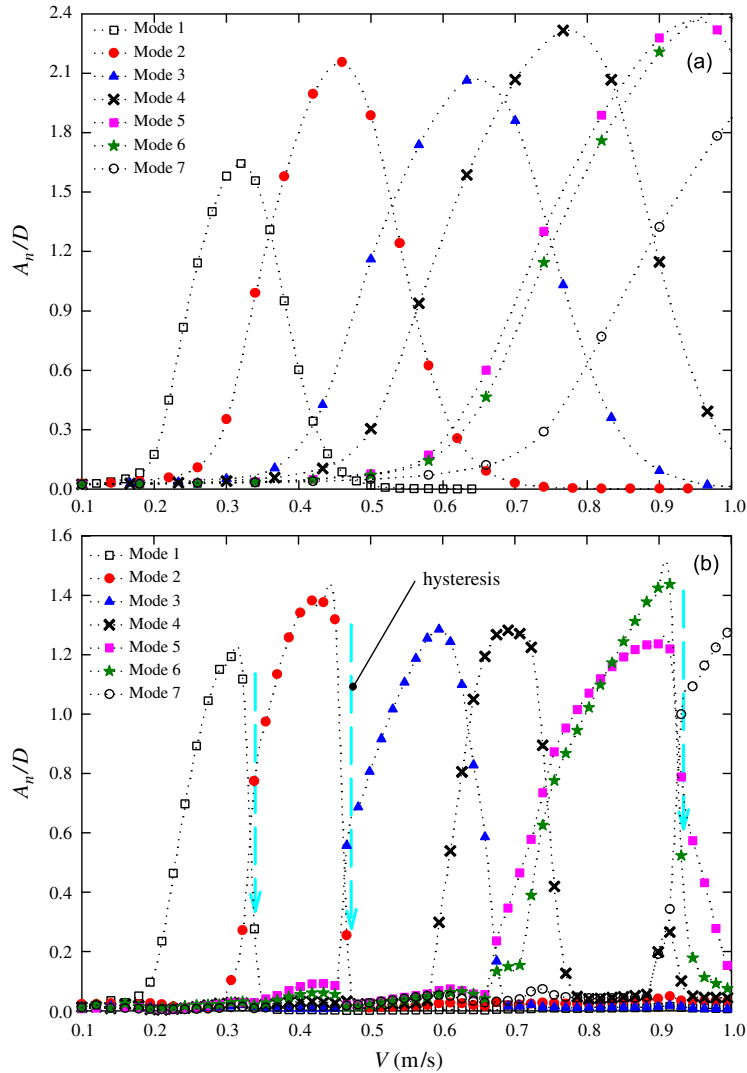
Fig. 4. Maximum modal amplitude diagrams of curved nonlinear cable with $N = 7$ ($n = 1$–7) and varying V: (a) single-mode versus (b) multi-mode models.

Corresponding to Fig. 4(b), Fig. 5 displays A_n/D versus the reduced flow velocity parameter $U_r = 2\pi V/\omega_n D$ based on each modal frequency ω_n. These plots are useful in comparing the extent of lock-in associated with different excited modes. Overall, the maximum A_n/D are in the range of $1 < A_n/D < 2$ and synchronization occurs in the range of $5 < U_r < 8$. These predictions of curved cable are in good quantitative and qualitative agreement with well-known cross-flow VIV characteristics of flexible cylinders (Fujarra et al., 2001).

To determine how many modes are actually required in obtaining a low-order multi-mode solution, it is necessary to perform a convergence study by varying N in the determination of A_R/D, which accounts for overall modal superimposition. The solution converges when A_R/D remains unchanged with increasing N. By considering the cable with $N = 2$ ($n = 1$–2), 3 ($n = 1$–3), 5 ($n = 1$–5), 7 ($n = 1$–7) and 9 ($n = 1$–9), the A_R/D are jointly plotted in Fig. 6 for $0.1 < V < 1$ m/s. It can be seen that the two- and three-mode models are only valid in the low V range ($V \leq 0.3$ m/s). More modes are required when further increasing V. With five-mode and seven-mode models, the solution convergence is satisfied in the higher ranges of $V \leq 0.5$ and 0.95, respectively, in comparison with the nine-mode model.

Overall, the mode switching with varying V, the multi-mode sharing and interactions whereby modal amplitudes overlap in different V ranges are systematically captured by the multi-mode model (Fig. 4(b)). A sufficient number of considered modes are required in the low-order model of flexible cylinder (Fig. 6). The single-mode model may lead to both quantitative as well as qualitative errors in VIV predictions (Fig. 4(a)). Therefore, it is suggested considering the
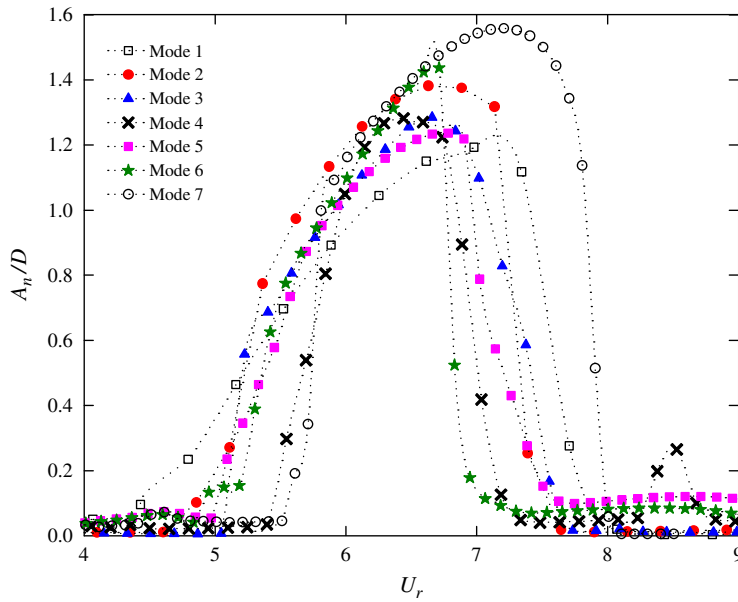
Fig. 5. Individual plots of maximum modal amplitudes versus U_r of curved nonlinear cable in Fig. 4(b) with $N = 7$ ($n = 1$–7).
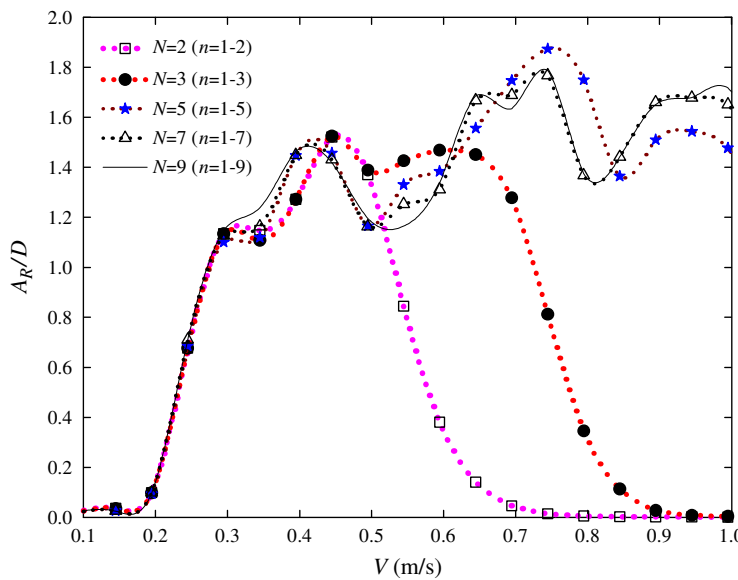

Fig. 6. Maximum total amplitude diagrams of curved nonlinear cable with varying N and V.

multi-mode model by simultaneously simulating all modal nonlinear differential equations. In the following, resonant nonlinear modes of flexible cylinder are discussed.

4.4. Resonant nonlinear modes of flexible cylinder

As highlighted in Sections 4.2 and 4.3, the multi-mode lock-in, sharing, switching and interaction features in VIV of flexible cylinder occur in a specific period of time and V range. Depending on modal characteristics (Fig. 2) and participating VIV amplitudes (Fig. 4(b)), the space–time varying profiles of u and v displacements are now constructed

based on Eq. (30) and normalized such that the spatially maximum amplitudes are equal to 1 (u_{nm}, v_{nm}). In the event of lock-in where vortex-shedding and cylinder oscillating frequencies are resonant, such displacement profiles are herein defined as ''resonant nonlinear modes'' of flexible cylinder. They are useful in the ensuing analyses of curvatures, stress and fatigue, and may be further useful in a framework of nonlinear modal reduction technique (Srinil and Rega, 2007).

Based on the A_n/D of inclined cable in Fig. 4(b) with $N = 7$, the u_{nm} (dashed lines) and v_{nm} (solid lines) profiles at different four time snapshots (t_1–t_4) are plotted in Fig. 7 for given $V = 0.339$, 0.595 and 0.739 m/s, respectively. With $V = 0.339$ m/s, there are two interacting 1st and 2nd modes in VIV with $A_1/D = 0.276$ and $A_2/D = 0.774$ (Fig. 4(b)). As a result, both u_{nm} and v_{nm} profiles exhibit either a predominant 1st-mode (t_1), 2nd-mode (t_2, t_3) or likely a combination of both (t_4), with respect to linear mode shapes in Fig. 2(a) and (b). The two-mode interaction feature is also shown when $V = 0.595$ m/s. In this case, the predominant modes are the 3rd and 4th modes with $A_3/D = 1.285$ and $A_4/D = 0.298$
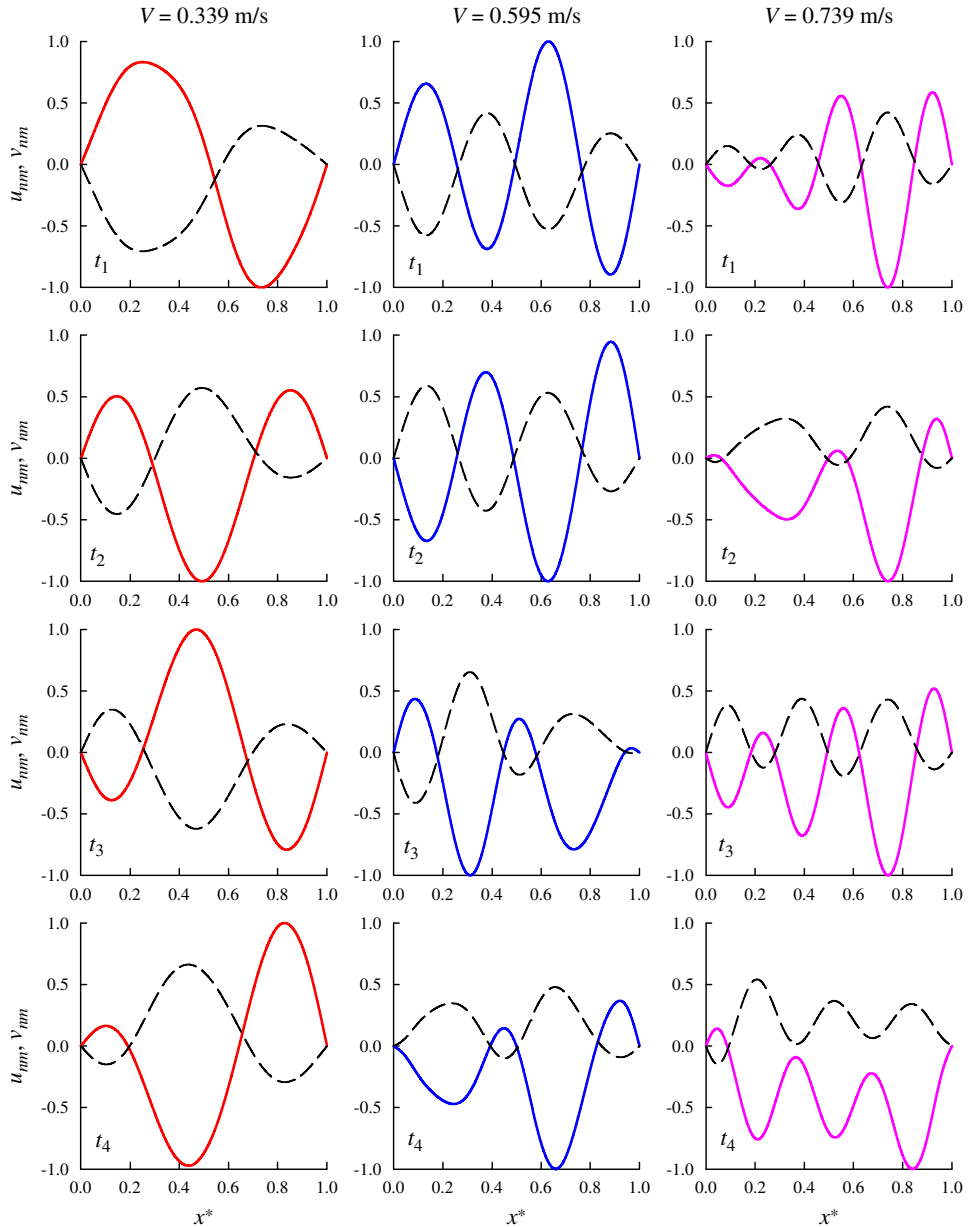

Fig. 7. Space–time varying displacement profiles with multi-mode superimposition and transition of curved nonlinear cable in Fig. 4(b) with $N = 7$ ($n = 1$–7) and three different V.

(Fig. 4(b)). Because of the much greater contribution from the 3rd mode than the 4th mode, resonant nonlinear modes are predominated by either the former (t_1, t_2) or the combination of both (t_3, t_4), whereas a pure 4th-mode response is not found. When further increasing V, the modal interaction effect becomes greater due to the increasing modal density at higher-order modes. This is highlighted by the three-mode interaction when $V = 0.739$ m/s. In this case, the nearly comparable participating amplitudes are $A_4/D = 0.894$, $A_5/D = 0.735$ and $A_6/D = 0.626$ (Fig. 4(b)). As a result, the asymmetry in nonlinear mode shapes is remarkable: the locations of minimum (node) and maximum (anti-node) amplitudes spatially and temporally vary. The largest curvatures appear near the seabed ($x^* = 1$) which is the region of primary concern in the design of curved cylinder such as catenary riser.

Hitherto, the attention has been placed on the analysis of the inclined cable due to the fact that a very few papers have investigated VIV of flexible curved cylinders. Yet, the methodologies applied to an inclined cable are the same as those applied to a straight beam. These should involve a complete study of time histories (Section 4.2), modal amplitudes (Section 4.3) and resonant nonlinear modes (Section 4.4), by also varying V and N. Owing to multi-mode interactions, nonlinear and linear modes are in fact different, since the former can vary with space and time. Depending on modal contributions, the space–time evaluation of cylinder maximum amplitudes is very useful as relevant experiments need a realistic positioning of strain sensors measuring the peak fatigue. In the following, the effects of fluid/structure parameters on VIV predictions are investigated, by considering all cable/beams with reasonable low-order models.

4.5. Influence of Reynolds number

It is now of importance to examine the influence of Re on multi-mode VIV predictions of flexible cylinders. In so doing, all curved cable and straight beams with geometric nonlinearities are analyzed, and the modal amplitudes (A_n/D) with Fixed- and Varied-FG models are compared. By accounting for the Re effect (Eq. (28)) in the derivation of wake coefficients, some varying F and G values with Re are given in Table 3 for cable/beam$_1$ and beam$_2$. Note that the sub-critical flow range is considered with the assumed maximum Re $\approx 3 \times 10^5$ (Sumer and Fredsøe, 2006). As Re increases, Table 3 shows that F slightly increases whereas G decreases more noticeably. This entails how the coupled wake/cylinder system is mostly controlled by damping terms in Eq. (16) which, in fact, regulate the self-limiting character in VIV. Thus, as G decreases (Re increases), it is expected to come across greater response amplitudes due to the diminishing damping effect, and this is consistent with the experimental results of Govardhan and Williamson (2006). By comparing between Tables 1 and 3, the fixed F and G (Skop and Balasubramanian, 1997) in Table 1 correspond to the estimated F and G in Table 3 in the Re $< 2.5 \times 10^4$ range.

It is worth mentioning that the formula in Eq. (28) is based on experimental forced vibrations of rigid cylinder in the range of $500 < \text{Re} < 3.3 \times 10^4$, and it is presently unknown whether this formula continues to be valid at higher Re (Govardhan and Williamson, 2006). Nonetheless, based on recent experimental results of flexible cylinder, Swithenbank et al. (2008) showed a significant trend of increasing amplitudes with Re up to 2×10^5. For this reason, it is herein assumed that Eq. (28) holds towards the upper limit of sub-critical flow range, with the aim of determining whether and how incorporating the Re dependence into the theoretical model could qualitatively and quantitatively affect the associated VIV predictions.

By considering now the inclined cable (beam$_1$) with $N = 9$, $0.1 < V < 1$ m/s and $3 \times 10^4 < \text{Re} < 3 \times 10^5$, Fig. 8(a) ((c)) and (b) ((d)) display the A_n/D diagrams with Fixed- and Varied FG models, respectively. It can be seen that both quantitative and qualitative differences occur between the two models neglecting or accounting for the Re effect (i.e., Fig. 8(a) versus (b) and Fig. 8(c) versus (d)). For both curved/straight cylinders, the amplitudes – as well as the

Table 3
Variation of wake coefficients with Re for considered curved/straight structures.

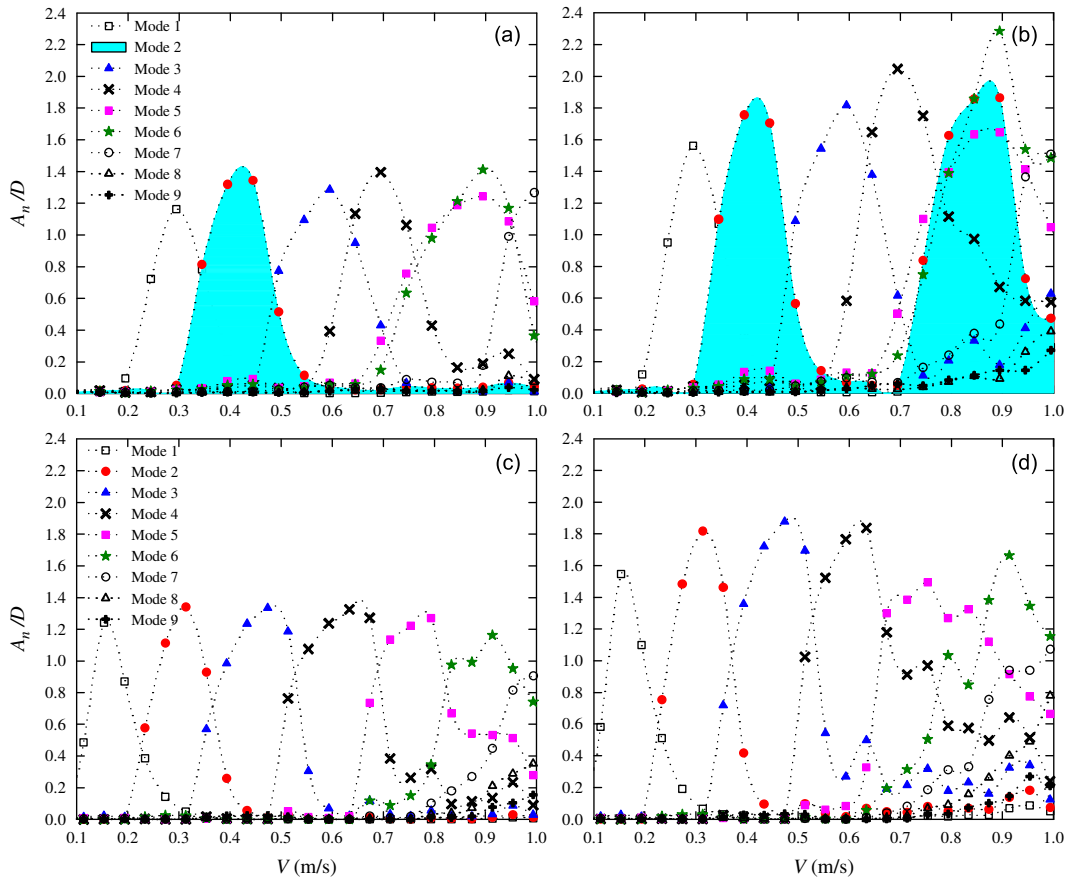| Re	Cable/Beam$_1$		Beam$_2$	
	F	G	F	G
5000	0.641	0.597	0.307	3.191
10000	0.644	0.470	0.315	2.267
25000	0.647	0.357	0.322	1.594
50000	0.648	0.297	0.326	1.278
75000	0.649	0.268	0.327	1.137
100000	0.650	0.251	0.328	1.052
250000	0.651	0.205	0.331	0.838
300000	0.651	0.197	0.331	0.804

Fig. 8. Maximum modal amplitude diagrams of (a, b) curved nonlinear cable and (c, d) nonlinear beam$_1$ with $N = 9$ ($n = 1$–9), varying V and models (b, d) accounting for or (a, c) neglecting the Re effect (i.e., (a) versus (b) and (c) versus (d)).

resulting modal interactions – predicted by the Varied-FG model become greater than those predicted by the Fixed FG model. This is expected from the decreasing G in Table 3. The maximum A_n/D of cable (beam$_1$) is about 1.41 (1.33) by the Fixed-FG model, whereas it reaches about 2.3 (1.88) by the Varied-FG model. Interestingly, for cable with Varied-FG model, the 2nd-mode is excited in two different – primary ($0.3 < V < 0.5$ m/s) and secondary ($0.7 < V < 1.0$ m/s) – lock-in regimes, as highlighted by the shaded areas in Fig. 8(b). In the secondary lock-in region, there are as many as six interacting modes in VIV responses. For instance, with $V = 0.845$ m/s (Re $\approx 2.5 \times 10^5$), the underlying modes are $A_2/D = 1.86$, $A_3/D = 0.33$, $A_4/D = 0.97$, $A_5/D = 1.63$, $A_6/D = 1.86$ and $A_7/D = 0.38$. These observed responses are in contrast to the Fixed-FG model (Fig. 8(a)) where only primary lock-in region of 2nd mode occurs (see the shaded area) and, with $V = 0.845$ m/s, there are fewer three excited modes with $A_4/D = 0.16$, $A_5/D = 1.19$ and $A_6/D = 1.21$.

The participation of 2nd mode in the curved cylinder response giving rise to its secondary lock-in regime at higher V may be attributed to the effect of 2:1 internal resonances since both ω_5 (2.168 rad/s) and ω_6 (2.228 rad/s) frequencies are nearly twice that of ω_2 (1.033 rad/s) (see Table 2). Both higher modes are in fact strongly coupled and can excite the lower one through geometric nonlinearities of initial curved structure (Srinil and Rega, 2007). Thus, the Varied-FG model in Fig. 8(b) highlights the occurrence of simultaneous external/internal resonances due to the interactions of cylinder versus vortex-shedding and cylinder versus cylinder frequencies, respectively. These numerical outcomes entail large-amplitude VIV predictions at high Re range, though relevant experimental confirmation is still unavailable.

When considering beam$_1$, the modal interaction effect again becomes more manifest as Re (G) increases (decreases), as shown by the Varied-FG model in Fig. 8(d) in comparison with the Fixed-FG model in Fig. 8(c). Nevertheless, the secondary lock-in of any mode is not observed. This is because, even though system natural frequencies are commensurable as integer ratios (Table 2), the nonlinear orthogonality properties of symmetric (e.g. 3rd) versus anti-symmetric (e.g. 6th) modes prevent the internal resonance from being activated (Srinil and Rega, 2007). Thus, the differences between Fig. 8(a) ((b)) and (c) ((d)) are due to the effect of varying initial curvatures of cable since other input parameters are identical (Table 1).
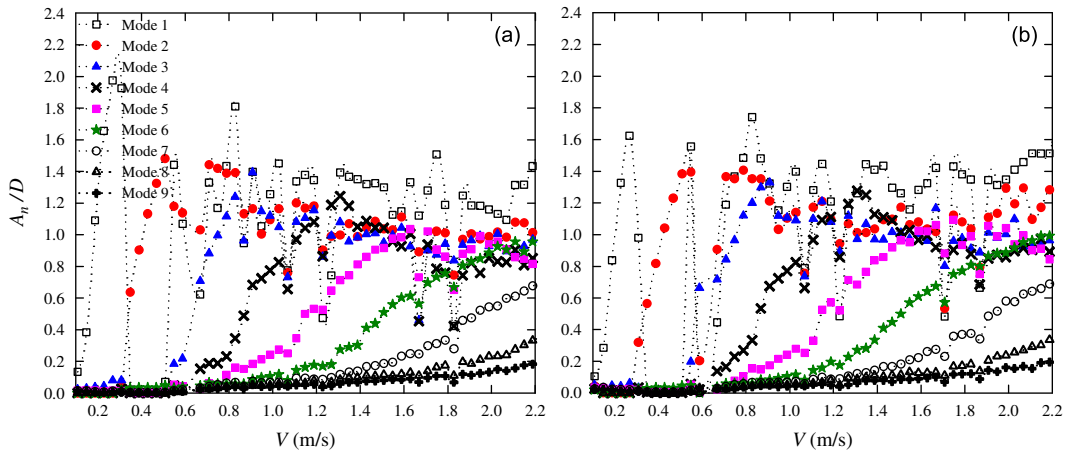
Fig. 9. Maximum modal amplitude diagrams of nonlinear $beam_2$ with $N = 9$ ($n = 1$–9), varying V and models (a) accounting for or (b) neglecting the Re effect.

$Beam_2$ which has a greater bending stiffness (Δ) than $beam_1$ is now considered with $0.1 < V < 2.0$ m/s and $2 \times 10^3 < Re < 3 \times 10^4$. The A_n/D results with $N = 9$ are plotted in Fig. 9. In contrast to $beam_1$, the Re effect on VIV prediction is seen to be relatively small for $beam_2$. Both Fixed-FG (Fig. 9(a)) and Varied-FG (Fig. 9(b)) models reveal similar A_n/D diagrams with a high degree of multi-mode contributions throughout the V range. With $V > 0.5$ m/s, there is no clear synchronization or lock-in condition found in either Fig.9(a) or (b), and the time histories are indeed non-periodic and highly modulated as illustrated by the first four modal (f_1–f_4) responses in Fig. 10 with $V = 1.11$ m/s (Fig. 9(b)). Recall also that $beam_2$ has high and widely spaced values of natural frequencies (Table 2). By considering a larger mass-damping parameter (α^*) with increasing either the mass (m^*) or damping (ξ) ratio, numerical results with Varied-FG model (not shown herein) still reveal non-periodic features although with smaller amplitudes. The occurrence of highly modulated responses of a straight beam in uniform flow has been observed, e.g., by Chaplin et al. (2005b). Recently, Chasparis et al. (2009) defined the non-periodic as chaotic response and suggested several excited modes in chaotic VIV. Based on available experiment results (Tognarelli et al., 2004), the validation of numerical results of $beam_2$ will be discussed in Section 4.7, by also recognizing the high fluctuating responses as in Fig. 10 and thus considering the rms amplitudes.

4.6. Influence of structural geometric nonlinearities

The influence of geometric nonlinearities on VIV predictions of flexible cylinders is now highlighted. By considering linear curved/straight cylinder models which disregard the modal interaction terms in Eq. (14), all inclined cable, $beam_1$ and $beam_2$ are again analyzed. With Varied-FG model and $N = 9$, the predicted maximum A_n/D are displayed in Fig. 11(a) (cable), (b) ($beam_1$) and (c) ($beam_2$), in comparison with nonlinear model results in Figs. 8(b), (d) and 9(b), respectively. Overall, there are quantitative and qualitative differences between nonlinear and linear models. In particular, the secondary lock-in regime of cable 2nd mode is not detected by the linear model in Fig. 11(a). This justifies how the observed 2:1 internal resonances in Fig. 8(b) are associated with geometric nonlinearities. With regard to beams, overall modal amplitudes ($A_n/D \approx 1.5$–2.5) in Fig. 11(b) ($beam_1$) and (c) ($beam_2$) are considerably greater than those in the associated Figs. 8(d) and 9(b) due to the neglected multi-mode interactions in the former. As a result, a single-mode lock-in is clearly seen throughout the V range in both Figs. 11(b) and (c). Because only the wake nonlinearities (Eq. (20)) are taken into account in the results of Fig. 11, the observed hysteresis effect in modal responses is solely associated with the fluid mechanism. This is in good qualitative agreement with experimental results by Brika and Laneville (1993).

By superimposing all modal amplitudes and accounting for their standard variations, the plots of A_{rms}/D versus varying V and x^* are now illustrated in Fig. 12, by comparing between nonlinear and linear models of cable (Fig. 12(a) versus (b)) and $beam_2$ (Fig. 12(c) versus (d)). Both Figs. 12(a) and (b) appear qualitatively similar in terms of overall amplitude variations although there are some differences in spatial profiles at high V (> 0.7 m/s) due to different modal contributions shown in between Figs. 8(b) and 11(a). On the contrary, both quantitative/qualitative differences in spatial profiles are remarkable for $beam_2$ when comparing between nonlinear (Fig. 12(c)) and linear (Fig. 12(d))
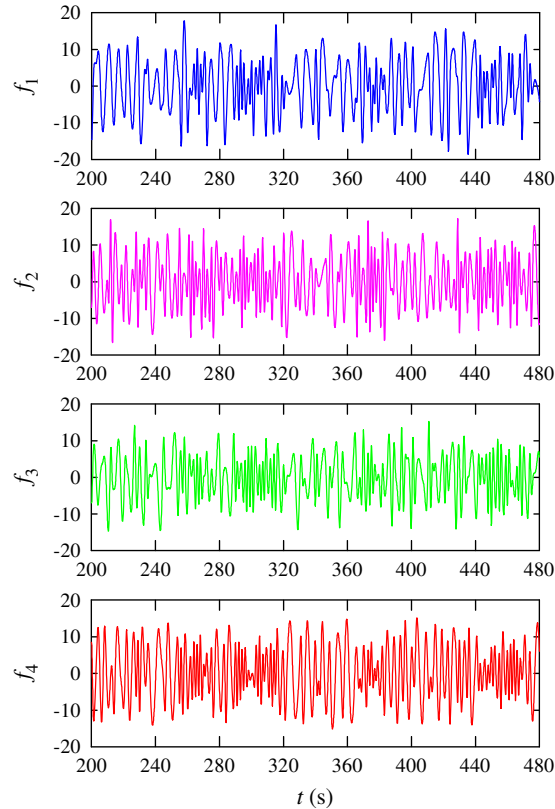
Fig. 10. Example of non-periodic and highly modulated modal responses of nonlinear beam$_2$ in Fig. 9(b) with $V = 1.11$ m/s.

cylinder models. The nonlinear (linear) model entails smaller (greater) $A_{rms,max}/D = 0.593$ (0.694). According to a single-mode lock-in feature in Figs. 11(c), Fig. 12(d) shows a regular pattern of spatial profiles with increasing number of half-sine waves as V and mode number increase. This is in contrast to Fig. 12(c) where a dominant mode cannot be characterized in a wide V range due to high multi-mode contributions and fluctuation of response amplitudes as shown in Figs. 9(b) and 10, respectively.

4.7. Numerical and experimental comparisons

The presented low-order wake/cylinder interaction model is now validated by performing numerical and experimental comparisons of VIV predictions. Owing to the varying modal interaction effect, the comparisons within a whole V range, rather than a specific V, should be made. In this study, the experimental results of beam$_2$ post-processed by Tognarelli et al. (2004) are referenced, by only considering cross-flow VIV. Of importance from a design viewpoint, the numerical–experimental comparisons are made in terms of spatially maximum values of rms amplitudes ($A_{rms,max}/D$) and "fatigue damage index" (FDI$_{max}$). Following Tognarelli et al. (2004), FDI may be approximated as FDI $\approx f_d \varepsilon^3$, where f_d is herein the natural frequency (Hz) of a mode predominating in VIV response and ε is the micro-bending strain calculated based on a rms value of cylinder dynamic curvature. Note that the estimation of fatigue damage is usually based on a ratio of the number of stress cycles incurred over the number of stress cycles to failure. This could be evaluated through the S–N curve which may entail the proportionality relationship: fatigue damage $\propto f_d \sigma^3$ (Baarholm et al., 2006). Because the stress (σ) is proportional to the bending strain that can be directly measured from experiments via strain gauges, Tognarelli et al. (2004) have introduced FDI to simply approximate the fatigue damage with a slope of 3 from S–N curve. This is convenient in the parametric studies and further comparisons with industrial tool predictions (Yang et al., 2008). In fact, the FDI is independent of a stress concentration factor or S–N curve intercept, but providing these values would give rise to actual fatigue damage being proportional to FDI by a constant factor.

In Fig. 13, both linear (L) and nonlinear (NL) structural models are analyzed, by also accounting for the Re effect (Varied-FG model). By varying V, Fig. 13(a) compares the variation of $A_{rms,max}/D$ with different low-order ($N = 8, 9, 10$)
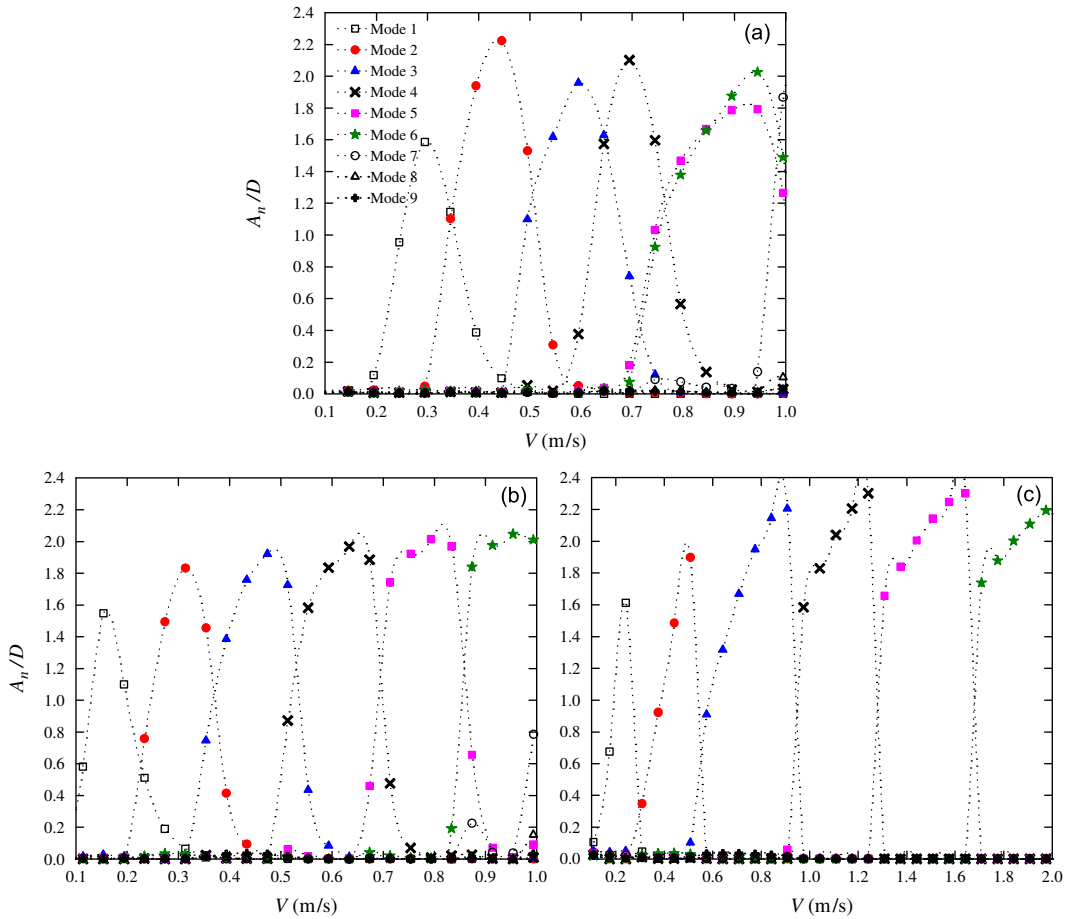
Fig. 11. Maximum modal amplitude diagrams of (a) curved cable, (b) beam$_1$ and (c) beam$_2$ with $N = 9$ ($n = 1$–9), varying V and neglected geometric nonlinearities.

models and with NL versus L ($N = 9$) models. Correspondingly, Fig. 13(b) compares the variation of FDI$_{max}$. It can be seen in Fig. 13(a) that, in a low V range, all numerical models yield good agreement with experiment results. For $V > 0.8$ m/s, the differences increase: the predicted amplitudes by NL models are lower than the experimental amplitudes whereas those by L model ($N = 9$) are more comparable to the latter. On the contrary, as V increases in Fig. 13(b), the L model provides considerably overestimated FDI$_{max}$ results whereas all NL models entail better quantitative predictions. Such greater discrepancies given by the L model increase with V and persist in spite of varying N, as shown in Fig. 13(c). Therefore, Fig. 13(a)–(c) highlight the effect of geometric nonlinearities on numerical predictions as well as their comparisons with experimental post-processed results.

Overall, Fig. 13(b) and (c) show how both numerically and experimentally predicted fatigue damage progressively increases with increasing V. A better quantitative comparison of FDI$_{max}$ between numerical NL model and experimental results is plausible since bending strains have been directly measured and used in the FDI approximations. This is in contrast to the experimental amplitudes whose values have been post-processed based either on double integrations of strains/ accelerations or a linear modal analysis in frequency domain. For this reason, a poorer (better) comparison of fatigue damage indices (response amplitudes) is found by the L model. Because such post-processing procedure for the estimated displacements overlooks the effect of geometric nonlinearities as well as multi-mode interactions, it may be more worthwhile relying on a comparison of bending strains or damage indices rather than amplitudes. Yet, quantitative errors are still seen by numerical results of NL model in Fig. 13(b) and these may be due to the wake oscillator's inability to capture actual flow mechanisms in the wake and to the fact that the considered low-order model excludes the effect of in-line VIV.

To show the possible effect of other input parameters, Fig. 13(d) compares $A_{rms,max}/D$ results with different given St, by considering the NL model with $N = 8$. Recall also that, in contrast to coefficients F and G, the St value is fixed when varying V (Re). The St effect on VIV prediction and comparison with experiment result is studied due to the fact that
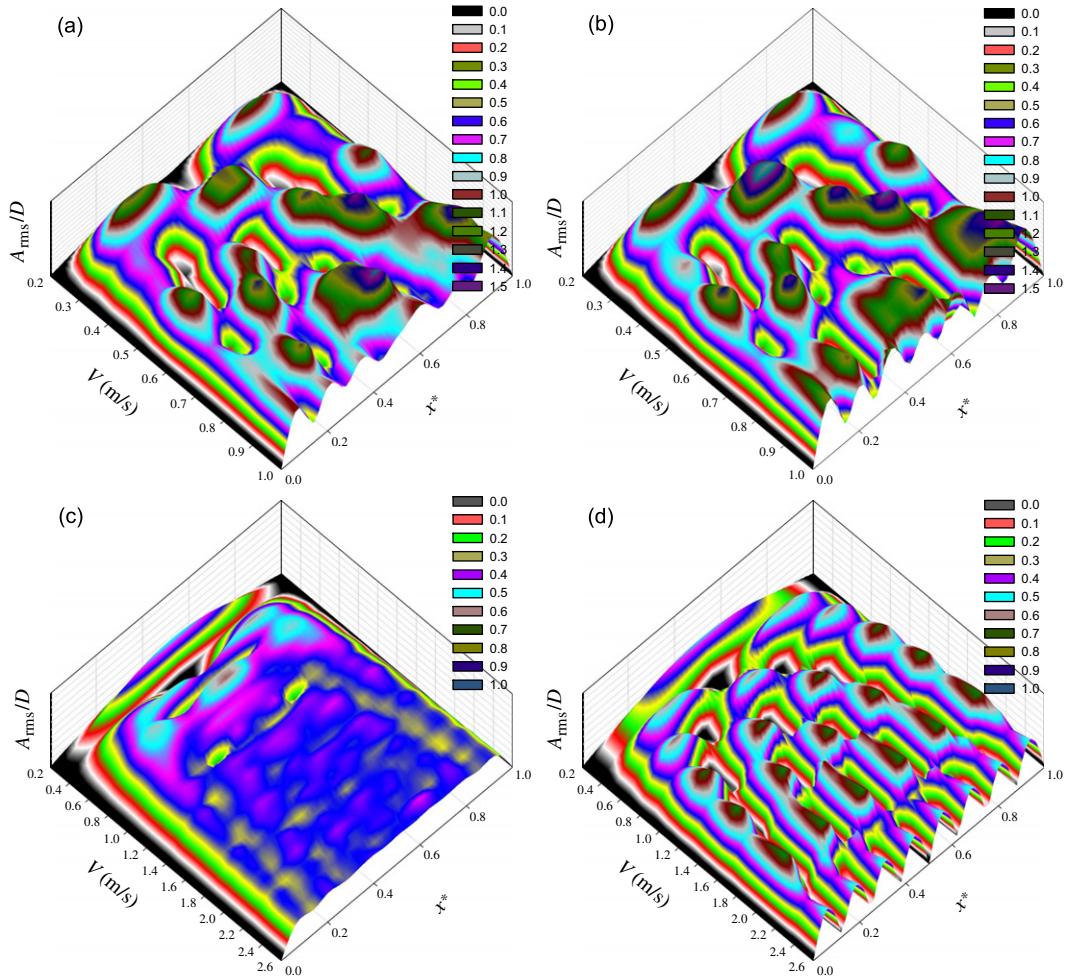
Fig. 12. Spatial variation of rms amplitudes with (a, c) nonlinear and (b, d) linear structural models of (a, b) curved cable and (c, d) beam$_2$ with $N = 9$ ($n = 1$–9) and varying V (i.e., (a) versus (b) and (c) versus (d)).

the reported St values in the literature are different though post-processing the same ExxonMobil experimental data. For instance, St = 0.21 in Tognarelli et al. (2004) whereas St = 0.14 in Yang et al. (2008). In Fig. 13(a)–(c), results are based on the averaged St = 0.17 (Table 1). Because St has been incorporated into theoretical model (implicitly through μ) and governing formulae (Eqs. (21)–(28)) deriving the varying wake coefficients, the predicted numerical results are influenced by St. Indeed, these are shown in Fig. 13(d) where, in a high V range, $A_{rms,max}/D$ increase with decreasing St and results with St = 0.14 become less quantitatively different from experimental results. This emphasizes that the accurately referenced value of St, apart from other influencing parameters (such as ξ and its mode dependence), is also important in the comparison of numerical and experimental predictions.

4.8. Discussion

To further improve numerical results and their comparisons with experimental data, some aspects on the VIV modelling and predictions of flexible curved/straight structures are summarized as follows:

(i) The effect of in-line motions which has been herein neglected should also be accounted for in the upcoming model development, since coupled cross-flow/in-line VIV are most realistic (Jauvtis and Williamson, 2004; Sarpkaya, 2004). Indeed, there are a very few wake oscillators for in-line VIV in the literature (Currie and Turnbull, 1987). For this reason, a new wake oscillator model for in-line VIV is needed along with its set of empirical coefficients.
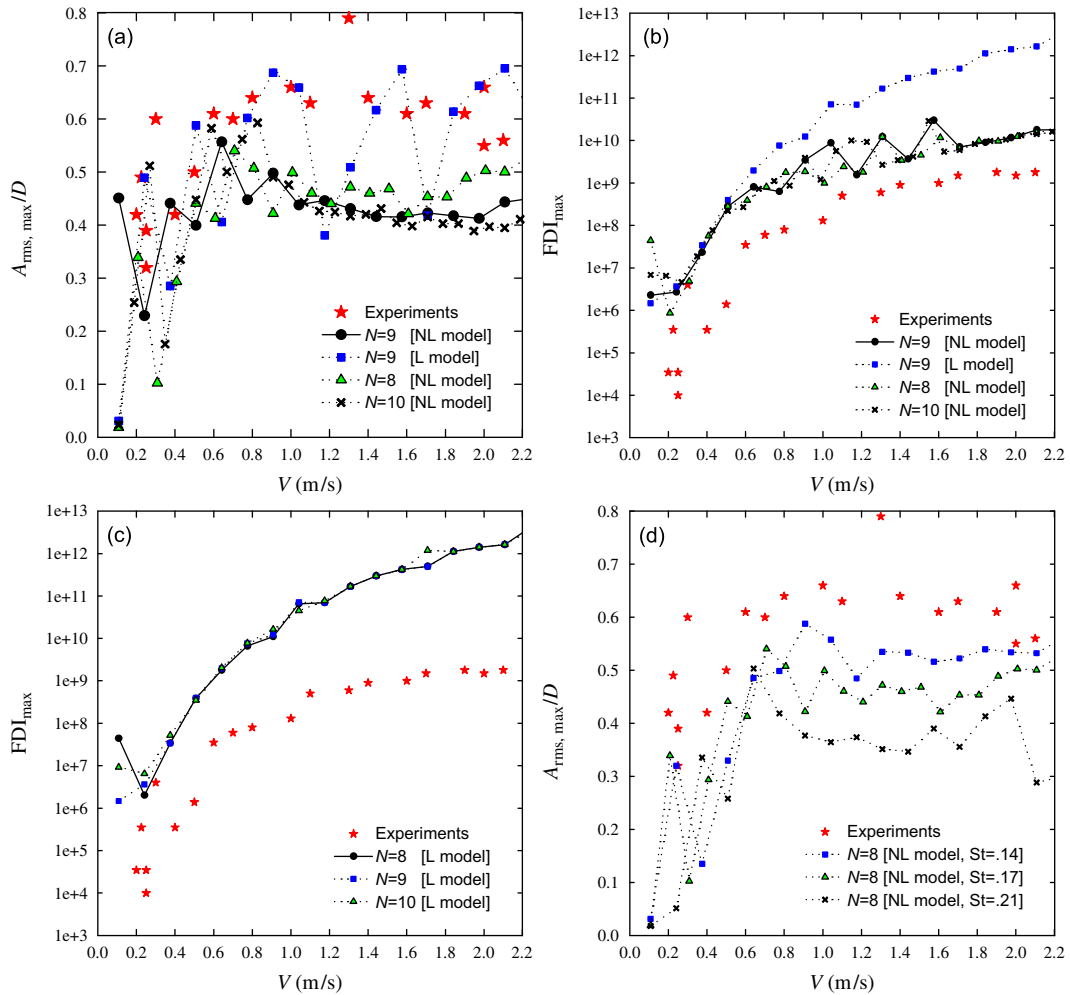
Fig. 13. Comparison of predicted numerical and post-processed experimental results of beam$_2$: (a) $A_{rms,max}/D$ with nonlinear (varying N) versus linear models; (b) FDI$_{max}$ associated with (a); (c) FDI$_{max}$ with linear model and varying N; (d) $A_{rms,max}/D$ with different St.

A complete study of cross-flow/in-line multi-mode VIV would allow us to identify the real extent of the underlying effects of geometric nonlinearities and multi-mode interactions.

(ii) As regards curved cylinder, the uniform flow perpendicular to its initial equilibrium plane has been herein considered. This is plausible because, in such a case, cross-flow wake dynamics of curved cylinder behaves qualitatively similar to those of straight cylinder (Miliou et al., 2003). To capture the effect of varying curvatures, the wake oscillator has been modified to account for the local angle between wake and cylinder axis. This might not be applicable to the case of flow being aligned with (or non-perpendicular to) the curvature plane where wake dynamics change dramatically, depending on the cylinder configuration being, e.g., convex or concave with respect to the incoming flow (Miliou et al., 2007). For flexible curved and inclined structures subject to non-perpendicular flows, the associated VIV dynamics have been found to be quite irregular and exhibit a hybrid standing-travelling wave behaviours with significant phase differences in motion along the structural axis (Moe and Teigen, 2004).

(iii) Depending on the number of interacting modes and system parameters, approximate closed-form solutions for the autonomous system Eqs. (13)–(16) may be derived based on, e.g., the method of multiple scales (Srinil et al., 2007). This would enlighten a variety of coexisting stable/unstable (periodic/chaotic) responses through bifurcations within the lock-in regimes. In addition, it would also be possible to determine a generic criterion on the minimum mode number required in the VIV analysis of flexible cylinders without performing time-consuming numerical simulations. The coexisting responses are practically useful in identifying a parametric range of unwanted dynamic scenarios leading to large-amplitude VIV, whereas the minimum mode number is theoretically important from a low-order modelling viewpoint.

(iv) On the other hand, it is worthwhile directly integrating the coupled Eqs. (4), (5) and (9) and (10) without modal expansion (Srinil and Rega, 2008b) to capture the actual infinite-dimensional nature of the distributed-parameter system and allow for the space–time modification of both fluid/structural properties. In so doing, a discrete x position where $\sin\theta = 0$ (Eqs. (9)) or $\cos\theta = 0$ (Eq. (10)) should be first examined. This is because, to avoid a breakdown during numerical simulations owing to the zeroing denominator, such x position will not be taken into account in the associated spatial discretization by, e.g., a finite difference approach.

(v) The empirical wake coefficients, even in the case of pure cross-flow VIV, could be further improved and calibrated with additional new experimental results. In particular, the formula (Eq. (28)) given by Govardhan and Williamson (2006) to capture the Re dependence should be validated whether it remains valid at high Re ($> 3.3 \times 10^4$) or a new formula should be proposed. In addition, it would be also worthwhile determining the Re dependence of the frequency ratio term given by Eq. (27). Numerical results in Section 4.6 have highlighted both quantitative and qualitative effects of Re on multi-mode VIV predictions of curved cylinder, and the relevant experimental investigations verifying these observations are also needed.

5. Summary and concluding remarks

Multi-mode interactions in VIV of flexible curved/straight cylindrical structures with geometric nonlinearities have been numerically investigated through a systematic low-order coupled wake-cylinder model. Cross-flow motions due to unsteady lift forces of inclined sagged cable and straight tensioned beams in uniform currents have been analyzed. The nonlinear equations of structural motions are based on a general pinned–pinned flexural curved cable model. The empirical hydrodynamic forces are based on the distributed van der Pol wake oscillators which capture both the effects of varying initial curvatures of inclined cylinder and Re. Numerical simulations have been performed in the case of varying flow velocities V. Depending on system fluid–structure parameters, empirical coefficients, vortex-shedding/ natural frequencies, modal characteristics, multi-mode contributions and assigned initial conditions, parametric results highlight several meaningful aspects of VIV of long flexible cylinders which have been experimentally observed in the literature. The main features are summarized as follows:

(a) Multi-mode lock-in, switching, sharing and interaction features take place both in response time histories (for a given V) and amplitude diagrams (with increasing V). In time histories, the beating phenomena with continuous amplitude modulations are observed in both cylinder/wake modal responses. In amplitude diagrams, multiple modal responses overlap in specific V ranges. The lock-in bandwidth and hydrodynamic added mass are found to be mode-dependent. The transition and superimposition of modes are displayed through the space–time varying displacement profiles which are herein defined as resonant nonlinear modes associated with lock-in conditions.

(b) Maximum modal and total amplitudes of flexible cylinders have been estimated. The lowest single-mode model may lead to quantitative as well as qualitative discrepancies when compared to multi-mode models. To obtain solution convergence of amplitudes, a proper number of potentially excited modes should be considered in low-order models.

(c) For inclined curved nonlinear cable, a new qualitative feature in VIV of flexible cylinder is found when accounting for the Re effect in the theoretical model and analysis. As V increases, simultaneous external/internal resonances – giving rise to both primary and secondary lock-in regimes – take place, with the secondary lock-in involving large-amplitude responses due to strong multi-mode interactions. For a tensioned beam with significant multi-mode contributions, the dynamic responses are highly non-periodic and modulated, and the Re is seen to play a minor role in response predictions.

(d) Overall, the geometric nonlinearities of flexible cylinders play a significant role both in VIV numerical predictions and comparisons with experimental results. The linear structural model provides overestimated modal amplitudes and ignores the meaningful effect of multi-mode interactions.

Apart from making use of a general low-order wake/cylinder interaction model and systematic approach in the analysis of flexible curved/straight structures undergoing multi-mode VIV, numerical results complement several experimental observations and furnish the improved understanding of multi-mode interaction features. The empirical wake oscillator could be further calibrated and modified in many ways along with new experimental and/or CFD-based hydrodynamics. It is felt that the presented low-order multi-mode model and numerical time-domain approach will be very helpful in the development of industrial prediction tools for the analysis and design of actual slender offshore structures involving hydrodynamic/geometric nonlinearities due to the space–time fluid/structure interactions.

Acknowledgements

References

Baarholm, G.S., Larsen, C.M., Lie, H., 2006. On fatigue damage accumulation from in-line and cross-flow vortex-induced vibrations on risers. Journal of Fluids and Structures 22 (1), 109–127.

Balasubramanian, S., Skop, R.A., Haan, F.L., Szewczyk, A.A., 2000. Vortex-excited vibrations of uniform pivoted cylinders in uniform and shear flow. Journal of Fluids and Structures 14 (1), 65–85.

Bearman, P.W., 2009. Understanding and predicting vortex-induced vibrations. Journal of Fluid Mechanics 634, 1–4.

Bishop, R.E.D., Hassan, A.Y., 1964. The lift and drag forces on a circular cylinder oscillating in a flowing fluid. Proceedings of the Royal Society Series A 277, 32–50.

Brika, D., Laneville, A., 1993. Vortex-induced vibrations of a long flexible circular cylinder. Journal of Fluid Mechanics 250, 481–508.

Chaplin, J.R., Bearman, P.W., Cheng, Y., Fontaine, E., Graham, J.M.R., Herfjord, K., Huera Huarte, F.J., Isherwood, M., Lambrakos, K., Larsen, C.M., Meneghini, J.R., Moe, G., Pattenden, R.J., Triantafyllou, M.S., Willden, R.H.J., 2005a. Blind predictions of laboratory measurements of vortex-induced vibrations of a tension riser. Journal of Fluids and Structures 21 (1), 25–40.

Chaplin, J.R., Bearman, P.W., Huera Huarte, F.J., Pattenden, R.J., 2005b. Laboratory measurements of vortex-induced vibrations of a vertical tension riser in a stepped current. Journal of Fluids and Structures 21 (1), 3–24.

Chasparis, F., Modarres-Sadeghi, Y., Hover, F., Triantafyllou, M., Tognarelli, M.A., Beynet, P., 2009. Lock-in, transient and chaotic response in riser VIV. In: Proceedings of the 28th International Conference on Offshore Mechanics and Arctic Engineering, OMAE2009-79444, pp. 1–7.

Currie, I.G., Turnbull, D.H., 1987. Streamwise oscillations of cylinders near the critical Reynolds number. Journal of Fluids and Structures 1 (2), 185–196.

Facchinetti, M.L., de Langre, E., Biolley, F., 2004. Coupling of structure and wake oscillators in vortex-induced vibrations. Journal of Fluids and Structures 19 (2), 123–140.

Farshidianfar, A., Zanganeh, H., 2010. A modified wake oscillator model for vortex-induced vibration of circular cylinders for a wide range of mass-damping ratio. Journal of Fluids and Structures 26 (3), 430–441.

Fujarra, A.L.C., Pesce, C.P., Flemming, F., Williamson, C.H.K., 2001. Vortex-induced vibration of a flexible cantilever. Journal of Fluids and Structures 15 (3–4), 651–658.

Gabbai, R.D., Benaroya, H., 2005. An overview of modeling and experiments of vortex-induced vibration of circular cylinders. Journal of Sound and Vibration 282 (3–5), 575–616.

Govardhan, R.N., Williamson, C.H.K., 2006. Defining the modified Griffin plot in vortex-induced vibration: revealing the effect of Reynolds number using controlled damping. Journal of Fluid Mechanics 561, 147–180.

Hartlen, R.T., Currie, G., 1970. Lift-oscillator model of vortex-induced vibration. Journal of Engineering Mechanics 96, 577–591.

Hover, F.S., Miller, S.N., Triantafyllou, M.S., 1997a. Vortex-induced oscillations in inclined cables. Journal of Wind Engineering and Industrial Aerodynamics 69–71, 203–211.

Hover, F.S., Miller, S.N., Triantafyllou, M.S., 1997b. Vortex-induced vibration of marine cables: experiments using force feedback. Journal of Fluids and Structures 11 (3), 307–326.

Iwan, W.D., Blevins, R.D., 1974. A model for vortex-induced oscillations of structures. Journal of Applied Mechanics 41, 581–586.

Jaiswal, V., Vandiver, J.K., 2007. VIV response prediction for long risers with variable damping. In: Proceedings of the 26th International Conference on Offshore Mechanics and Arctic Engineering, OMAE2007-29353, pp. 1–9.

Jauvtis, N., Williamson, C.H.K., 2004. The effect of two degrees of freedom on vortex-induced vibration at low mass and damping. Journal of Fluid Mechanics 509, 23–62.

Kim, W.J., Perkins, N.C., 2002. Two-dimensional vortex-induced vibration of cable suspensions. Journal of Fluids and Structures 16 (2), 229–245.

Larsen, C.M., Halse, K.H., 1997. Comparison of models for vortex induced vibrations of slender marine structures. Marine Structures 10 (6), 413–441.

Lie, H., Kaasen, K.E., 2006. Modal analysis of measurements from a large-scale VIV model test of a riser in linearly sheared flow. Journal of Fluids and Structures 22 (4), 557–575.

Miliou, A., de Vecchi, A., Sherwin, S.J., Graham, J.M.R., 2007. Wake dynamics of external flow past a curved circular cylinder with the free stream aligned with the plane of curvature. Journal of Fluid Mechanics 592, 89–115.

Miliou, A., Sherwin, S.J., Graham, J.M., 2003. Fluid dynamic loading on curved riser pipes. Journal of Offshore Mechanics and Arctic Engineering 125, 176–182.

Moe, G., Teigen, T., 2004. Predictions and model tests of a SCR undergoing VIV in flow at oblique angles. In: Proceedings of the 23rd International Conference on Offshore Mechanics and Arctic Engineering, OMAE2004-51563, pp. 1–12.

Nayfeh, A.H., 2000. In: Nonlinear Interactions: Analytical, Computational, and Experimental Methods. John Wiley & Sons, New York.

Norberg, C., 2003. Fluctuating lift on a circular cylinder: review and new measurements. Journal of Fluids and Structures 17 (1), 57–96.

Sarpkaya, T., 2004. A critical review of the intrinsic nature of vortex-induced vibrations. Journal of Fluids and Structures 19 (4), 389–447.

Skop, R.A., Balasubramanian, S., 1997. A new twist on an old model for vortex-excited vibrations. Journal of Fluids and Structures 11 (4), 395–412.

Srinil, N., Rega, G., 2007. Two-to-one resonant multi-modal dynamics of horizontal/inclined cables. Part II: Internal resonance activation, reduced-order models and nonlinear normal modes. Nonlinear Dynamics 48 (3), 253–274.

Srinil, N., Rega, G., 2008a. Nonlinear longitudinal/transversal modal interactions in highly extensible suspended cables. Journal of Sound and Vibration 310 (1–2), 230–242.

Srinil, N., Rega, G., 2008b. Space–time numerical simulation and validation of analytical predictions for nonlinear forced dynamics of suspended cables. Journal of Sound and Vibration 315 (3), 394–413.

Srinil, N., Rega, G., Chucheepsakul, S., 2007. Two-to-one resonant multi-modal dynamics of horizontal/inclined cables. Part I: Theoretical formulation and model validation. Nonlinear Dynamics 48 (3), 231–252.

Srinil, N., Wiercigroch, M., O'Brien, P., 2009. Reduced-order modelling of vortex-induced vibration of catenary riser. Ocean Engineering 36 (17–18), 1404–1414.

Sumer, B.M., Fredsøe, J., 2006. In: Hydrodynamics Around Cylindrical Structures. World Scientific.

Swithenbank, S.B., Vandiver, J.K., Larsen, C.M., Lie, H., 2008. Reynolds number dependence of flexible cylinder VIV response data. In: Proceedings of the 27th International Conference on Offshore Mechanics and Arctic Engineering, OMAE2008-57045, pp. 1–9.

Tognarelli, M.A., Slocum, S.T., Frank, W.R., Campbell, R.B., 2004. VIV response of a long flexible cylinder in uniform and linearly sheared currents. Offshore Technology Conference, OTC-16338, pp. 1–12.

Tognarelli, M.A., Taggart, S., Campbell, M., 2008. Actual VIV fatigue response of full scale drilling risers: with and without suppression devices. In: Proceedings of the 27th International Conference on Offshore Mechanics and Arctic Engineering, OMAE2008-57046, pp. 1–13.

Trim, A.D., Braaten, H., Lie, H., Tognarelli, M.A., 2005. Experimental investigation of vortex-induced vibration of long marine risers. Journal of Fluids and Structures 21 (3), 335–361.

Vandiver, J.K., Jaiswal, V., Jhingran, V., 2009. Insights on vortex-induced, traveling waves on long risers. Journal of Fluids and Structures 25 (4), 641–653.

Violette, R., de Langre, E., Szydlowski, J., 2007. Computation of vortex-induced vibrations of long structures using a wake oscillator model: comparison with DNS and experiments. Computers & Structures 85 (11–14), 1134–1141.

Violette, R., de Langre, E., Szydlowski, J., 2010. A linear stability approach to vortex-induced vibrations and waves. Journal of Fluids and Structures 26 (3), 442–466.

Willden, R.H.J., Graham, J.M.R., 2003. Multi-modal vortex-induced vibrations of a vertical riser pipe subject to a uniform current profile. European Journal of Mechanics—B/Fluids 23 (1), 209–218.

Williamson, C.H.K., Govardhan, R., 2004. Vortex-induced vibrations. Annual Review of Fluid Mechanics 36, 413–455.

Yang, G., Frank, W.R., Campbell, R.B., Slocum, S.T., 2008. VIV model test data comparison with Shear7 v.4.5. In: Proceedings of the 27th International Conference on Offshore Mechanics and Arctic Engineering, OMAE2008-57108, pp. 1–12.